HEAT, MOISTURE, AND MOMENTUM BUDGETS FOR AN OKLAHOMA SQUALL LINE

by

JUDITH STOKES

B.A., Clark College of the Atlanta University Center
1974

SUBMITTED IN PARTIAL FULFILLMENT
OF THE REQUIREMENTS FOR THE
DEGREE OF MASTER OF
SCIENCE
at the
MASSACHUSETTS INSTITUTE OF
TECHNOLOGY
JUNE, 1976

Signature of Author. . . . . .
Department of Meteorology, May 7, 1976

Certified by. . . . . .

Accepted by. . . . . .
Chairman, Departmental Committee

Heat, Moisture, and Momentum Budgets for an Oklahoma Squall Line

by

Judith Stokes

Submitted to the Department of Meteorology on May 7, 1976, in partial fulfillment of the requirements for the degree of Master of Science.

ABSTRACT

A squall line, which passed through the National Severe Storms Laboratory mesonetwork in Oklahoma on 26 April 1969, is analyzed to determine the interaction between cumulus elements and the mean mesoscale atmosphere, by examining the mesoscale circulation and obtaining cumulus effects as residuals in the budgets of heat, moisture, and momentum. The analyses are based on data from 23 rawinsonde ascents to the 400-mb level, 29 automatically surface recording stations, and radar PPI coverage.

The squall-line thunderstorms first appeared behind a surface cold front, formed a uniform line, and then moved out ahead of the front.

Analysis of the surface data showed that the surface wind shift and the temperature break associated with the gust front had a curve-shaped pattern and these two events were overtaken by the onset of rain in the northern part of the network.

A composite analysis of all the data revealed the existence of a mesoscale downdraft-updraft doublet in the vertical motions pattern. The downdraft is centered at about 10 km ahead of the leading edge of the radar echo line and the updraft centered at about 5 km behind the line. The downdraft appears to be driven by evaporative cooling from the tops of cumulus clouds and cooling due to the dissipation of a middle cloud layer; the updraft is driven by condensational heating and superimposed convection.

On the basis of this and other cases it is tentatively concluded that this doublet of mesoscale vertical motions may be a distinguishing feature of large convective storm systems in their mature stages of developement whether they be of frontal or of squall-line character.

Thesis Supervisor: Frederick Sanders
Title: Professor of Meteorology

TABLE OF CONTENTS

LIST OF ILLUSTRATIONS

1. Introduction

Some weather systems are too small to be followed in the standard synoptic network, yet produce profound results. Such organized systems as squall lines, masses of thunderstorms, sea-breeze systems, and large precipitation cells are in this category. They are said to be mesoscale phenomena (Byers, 1974).

Since the establishment of the rawinsonde mesonetwork at the National Severe Storms Laboratory (NSSL) in Oklahoma in 1966, it has been possible to study the mesoscale aspects of convective storm systems using a large number of vertical soundings together with a recording surface network, instrumented aircraft, and radar surveillance. Barnes et al. (1971) describe the archived soundings at NSSL for the years 1966 through 1970.

Some recent studies have made use of the NSSL rawinsonde data. Lewis et al. (1974) analyzed a case to determine the synoptic-scale influence upon squall-line generation. Fankhauser (1974) examined the squall-line case of 8 June 1966 to derive horizontal height perturbations dynamically consistent with mesoscale wind patterns in the presence of a well-organized squall line. The most intensive use of the NSSL rawinsonde data was made by Sanders and Paine (1975), hereafter referred to as S & P. Their examination of a frontal disturbance was directed toward studying the interaction between cumulus elements and the mesoscale pattern of motion.

Little research has been directed toward the study of the interaction of these two scales. Most studies have been concerned with the effects of tropical convection upon the synoptic scales (Yanai et al., 1973; Ogura and Cho, 1973). The present examination of the 26 April 1969 squall-line case (documented at NSSL) is addressed to the interaction between cumulus elements and the mean mesoscale atmosphere, by determining the mesoscale circulation and obtaining the cumulus effects as residuals in the budgets of heat,

moisture, and momentum.

On 26 April 1969 a squall line formed in the vicinity of a slow moving cold front in northwestern Oklahoma. The line strengthened during the day and moved east-southeastward ahead of the front through the 2700 square-kilometer mesonetwork area of NSSL. During the squall line's passage through the network much data was assembled, including observations from 29 automatically recording surface stations, vertical soundings from 29 rawinsonde ascents, and Plan Position Indicator (PPI) radar coverage at elevations from 0 to 18 deg. This storm system can be classified as severe, since it produced hail of up to 1.75 inches in diameter and spawned one known tornado.

Presented in the following sections are the description of the 1969 NSSL mesonetwork and data, the synoptic-scale events associated with the storm system, the results of analysis performed on mesoscale data, and the results of budget calculations.

2. Description of the 1969 NSSL mesonetwork and data

The 1969 NSSL mesonetwork is shown in Fig. 1. The surface network consisted of 29 stations with a mean spacing of about 8 km. These automatically recorded wind, temperature, relative humidity, pressure, and rainfall on strip charts and the sites were battery-powered to prevent loss of data during commerical power outages (Barnes et al., 1971). Eight rawinsonde sites, indicated by darkened circles in Fig. 1, operated in 1969. Soundings usually terminated at 400 mb. For this case 29 soundings were launched over a time period from 1400 to 1755 CST. Of these soundings, 23 were actually used in the study. Unfortunately only 16 of the remaining 23 had complete data from the surface up to 400 mb.

Radar coverage was provided by a modified WSR-57 10 cm radar at the NSSL headquarters, surface station 5E. Following electronic processing, power received from precipitation is displayed in range-azimuth coordinates on a PPI. Boundaries between two shades of gray and black (echo cancellation) depict constant reflectivity contours. These values, for even-numbered frames on the radar film, are given in Table 1 along with the coded values that are used in this paper (Zittel, 1976). For odd-numbered frames the reflectivity values are increased by 5 dBz and the coded values are increased by .5. Continuous PPI coverage is available from 0800 to 1815 CST for the 26 April case. The elevation angle is normally zero but an automatic sequence can be initialized at regular intervals in which the elevation angle is increased by 1 or 2 deg on each sweep to a maximum elevation angle of 18 deg. Following the highest elevated sweep the elevation angle returns to zero.

3. Synoptic-scale situation

Figure 2 shows the synoptic weather pattern for 0600 CST, 26 April 1969. In the surface analysis a cold front, associated with a closed low in the Dakotas, extends southwestward into northwestern Oklahoma and northern Texas. Ahead of the front the low-level flow is generally from the south-southeast, and is transporting warm moist air from the Gulf of Mexico into the northern Texas-central Oklahoma region.

The 400-mb analysis shows a deep short-wave trough extending from North Dakota southwestward into New Mexico. NSSL is located in a position between upper-level trough and downstream ridge, in a region of strong southwesterly flow. This location indicates synoptic-scale ascent is occurring over NSSL.

The soundings taken at Tinker Air Force Base (near the eastern edge of NSSL) on April 26, show that conditions were favorable for convective activity. The morning and afternoon temperature and dew-point soundings are illustrated in Fig. 3. At 0600 CST the soundings reveal a moist layer from 950 up to 850 mb. Within the layer the equivalent-potential temperature is uniformly near 325 deg K. This moist layer is surmonted by a dry potentially unstable layer that extends to 750 mb, above which the temperature distribution of the air column as a whole indicates conditional instability. Note the considerable amount of vertical wind shear and veering of the winds with height. All these conditions are favorable for severe convective activity (Fawbush et al., 1951; Browning, 1964).

By 1800 CST heavy thunderstorms and frequent lightning were reported. The temperature and dew-point soundings indicate an extremely moist layer from 950 up to 700 mb. The vertical wind shear is somewhat more pronounced than earlier.

The surface analysis 24 hours later (Fig. 4) shows that the front has advanced about 220 km, indicating an average rate of advance of about 9 km hr^{-1}. There is evidence of a squall line in the warm trough ahead of the front in central Texas, where the wind shift from south-southeast to northwest is distinct and some stations are reporting heavy thunderstorms.

An examination of the hourly reports from regular surface weather stations in Oklahoma and the radar film show that the thunderstorm activity on 26 April had become well organized into a line by 1500 CST. The formation of this line, its position relative to the surface front, and hourly surface synoptic-scale weather was investigated by reviewing a sequence of three-hourly surface maps (prepared using data from the surface stations) and a corresponding sequence of radar displays. The surface maps for 0900, 1200, 1500 and 1800 CST are shown in Fig. 5 and the corresponding radar displays in Fig. 6. The position of the leading edge of the squall line on the surface maps was in part determined from radar data and in part from the hourly time series at individual stations.

Most stations in Oklahoma reported overcast skies all day. Prior to 0800 CST none of the stations reported any thunderstorm activity. The surface map at 0900 CST is shown in Fig. 5a. Ahead of the cold front temperatures are near 65 deg F and winds generally from the south-southeast. The one station behind the front has a temperature of 48 deg F and the wind has shifted to northeast. A thunderstorm was at this station in the past hour. The radar display at 0900 CST shows an intense echo northwest (north being directed toward the top of the page) of NSSL near the left edge of Fig. 6a which could have possibly been over the station in the last hour. The echoes at the western edge of the network did not progress

through it but moved north of it. In fact, none of the echoes which appear on this display were associated with the squall line which later passed through the network.

By 1200 CST four of the stations ahead of the front are reporting thunderstorm activity. Radar echoes are over the two stations which are reporting thunderstorms at the time of observation. Note that the echoes ahead of the front (the average position of the surface front is indicated by the straight line on the radar display) west of the mesonetwork are not associated with the echoes that were slightly forward of this position in Fig. 6a. The latter echoes moved northward while the former moved here from the south. No distinct line of echoes has formed yet, however the weak echoes, which are just entering the range of the radar west-northwest of NSSL, are the beginnings of the line which passed through the network.

In Fig. 5c is the surface analysis for 1500 CST. The analysis shows the development of a small surface wave and at the same time the radar displays an organized squall line that is moving ahead of the surface cold front. The most intense part of the line, reflectivities as high as 62 dBz, is southwest of NSSL.

The squall line is well ahead of the front by 1800 CST and has passed through the mesonetwork. The front, along which no echoes are now found, is just entering the western edge of the network.

So it appears that the squall-line thunderstorms did not appear spontaneously in the warm air ahead of the front but first appeared behind it, formed a uniform squall line, and then moved out ahead of the front. This kind of squall-line development is similar to that described by Newton (1950). Since the cold front moves with a speed nearly that of

low-level winds, and the air near the squall line derives its momentum from higher levels where stronger winds prevail, it follows that the squall line must move at a rate faster than the cold front.

4. Mesoscale situation and organization of data

As shown in the previous section a portion of the squall line migrated through the NSSL mesonetwork between 1500 and 1800 CST. Thus it was possible to attempt to study the mesoscale structure of the storm system.

The temperature traces, in general, displayed a dual temperature break. A temperature break is defined here as the point on the trace at which the temperature begins to fall sharply. The first break, associated with the leading edge of the cold air outflow from the line of thunderstorms (the gust front), was very sharp. Temperatures were near 66 deg F and dropped to about 58 deg F in 10 min. The second break, which occurred about 2 hours later and was associated with cold-frontal passage, was not as sharp as the first and not clearly defined at all stations. Shown in Fig. 7 are the temperature and rainfall traces recorded at surface station 2C. The dual temperature break is apparent, and the onset of rain begins about 5 min before the first break.

Isochrones of the first temperature break and of the actual leading edge of the radar echo line (defined here as a slightly smoothed line centered between the first and second reflectivity contours at the leading edge of the echo area) are presented in Fig. 8. It is interesting to note that the break exhibits a curve-shaped pattern and it arrives in the northern part of the network later than it does in the southern part. At the same time, the leading edges of the radar echoes are more nearly straight. This structure is probably present because a strong southwesterly flow, 35 m sec^{-1}, is transporting the precipitation aloft, while a much weaker flow near the surface, 10 m sec^{-1}, is transporting the cold air.

Isochrones of the arrival of the first westerly component in the wind direction is shown in Fig. 9. The kind of pattern that was present in the temperature analysis is also here. At most stations the shift in

the wind direction occurred a few minutes ahead of the first temperature break. Before the westward shift the winds were generally from the south-southeast with speeds between 8 and 10 m sec^{-1}. After the shift the stations in the northern portion of the network showed a decrease in speeds, while the stations farther south showed an increase in speeds followed by a decrease. Cold-frontal passage at most stations was marked by the appearance of a northerly component in the wind direction, which occurred some two hours after the appearance of the first westerly component.

Isochrones of the onset of rain are presented in Fig. 10. The analysis shows that the rain ran out ahead of both the temperature break and the wind shift in the northern part of the network for the reason mentioned above. In Fig. 11 is the map of the total rainfall recorded on 26 April 1969. The heaviest, 1.25 inches, was recorded at stations 7A and 6C in the southwestern part of the network. The most severe weather recorded within the network occurred near this region. Hail of up to 1.75 inches in diameter was reported at Blanchard (BLA) around 1715 CST and a tornado touched down near the Tabler community (see Fig. 11) about 1700 CST (U.S. Department of Commerce, 1969).

The radar echo from a tornadic storm often displays a hook-shaped appendage (Davies-Jones and Kessler, 1974). The Tabler tornado exhibits this feature. The development of this hook echo as well as a brief history of the squall line during the time it was within the surface network can be summarized by viewing the half-hour interval sequence of PPI film shown in Fig. 12.

At 1600 CST the line is entering the western edge of the network and has an average width of about 35 km. The most intense part of the line, log Z_e = 6.2, passes through the network. As pointed out in Fig. 12a

the hook echo develops to the lower right of this high reflectivity region.

By 1630 CST the line has progressed over halfway through the network. The northern part of the line has broken away from the main line. The place where the hook echo forms is again pointed out. Fig. 12c shows that the entire width of the line is within the network and has entered into the ground clutter of the radar. The hook-shaped appendage, on the right of the most intense echo region, is clearly visible now and is over the Tabler area. The northern portion of the line has moved farther away.

The arrangement of the radar echoes in a line as they passed through the mesonetwork is apparent in all the above displays. Isochrones of the progress of the actual leading edge of radar echoes through the network are shown in Fig. 8. Since these lines are more nearly straight than the isochrones of the temperature break and the wind shift we chose to study this system in a frame of reference relative to the leading edges of the radar echoes. Here we define a smoothed average leading edge of the radar echo line, hereafter referred to as LERE, as a straight line moving at a constant speed of .53 km min^{-1}, lying usually between the first and second reflectivity contours. Fig. 13 shows the advance of the LERE line through the network and a coordinate system moving with the line. A detailed explanation of this coordinate system is given in the Appendix.

The vertical structure of the storm system, as detected by radar, was investigated by constructing vertical cross-sections from the PPI echoes at elevated antenna angles from 1 to 18 deg along azimuth 297 through station 5E. A vertical cross-section was prepared for seven scans. These sections were then composited into one. An analysis was done on the number of scans, out of the seven, which had non-zero reflectivity values at a given point. The 1- and 6- lines taken from this analysis are

illustrated as dashed lines in Fig. 14. The abscissa is labelled in terms of both time and distance relative to the LERE. The most intense echo region extends from about 5 km ahead of to about 20 km behind the LERE. Also shown in Fig. 14 are the projections of the paths of the rawinsonde balloons on the y(t) -p plane.

We found that with only 23 soundings the data is too sparse to permit the representation of significant meteorological variables (horizontal wind components, mixing ratio, and potential temperature) in all three spatial dimensions and in time. But the organization of the storm system into a well-defined line and the short time span of the observational period suggest preparation of a composite analysis of the rawinsonde data based on the assumptions of a steady state and of no variation in the direction parallel to the LERE. Therefore, the variables were analyzed and the results are presented in a vertical plane transverse to the LERE. However, lack of data prohibited the measurement of variations in time, so it is not known whether the assumption of steady state is valid. Because of a strong south-southwesterly flow, the assumption of no variations along the LERE is not valid in budget calculations. Nevertheless, the results are still presented in a plane transverse to the LERE since this presentation makes best use of the data.

In order to avoid inclusion of small irregularities in the analysis of the rawinsonde data, 50-mb means of all pertinent meteorological variables are used, as suggested by Fankhauser (1974). Note that the mean for the lowest layer, from the surface pressure to 950 mb, represents a thickness of only about 9 mb. These mean values are attributed to the mid-pressure of the layer. Details about the processing of the rawinsonde data are described in the Appendix.

As shown in Fig. 14 of the five attempts to launch a balloon in the most intense echo region only one reached 400 mb. A comparison of this sounding with ones nearby showed that above 525 mb its rate of ascent, mixing ratio, and equivalent-potential temperature were higher, indicating it probably entered an active convective updraft above 525 mb. The crashes were either due to flight equipment failure or precipitation and icing on the balloons. This lack of data in the intense echo region presented problems in the analysis that will be discussed later.

5. Distribution of meteorological variables

a. horizontal wind components

The components of wind along the x and y axes of the coordinate system shown in Fig. 13 are denoted by u and v, respectively. Shown in Fig. 15 is the u component of the wind. Note the strong vertical shear in a low-level jet-stream region near the surface. While isolated cumuli are often seen to be torn apart when subjected to strong vertical shear, squall lines and large thunderstorms causing severe weather are thought to show a preference for the jet-stream region where there is strong vertical shear (Newton, 1963).

The field presents a strong south-southwesterly wind component throughout the whole region except in the lower layers on the left, where the strength has decreased somewhat. In this respect this case differs radically from the one studied by S & P, where the component of wind along the front was quite small. This strong south-southwesterly flow is the main reason why the two-dimensional display in the y(t) - p plane presented here cannot fully describe this three-dimensional system, that is, advections $- u \frac{\partial Q}{\partial x}$ are not negligible because of large values of u. However, as stated before, because of spareness of data this type of display makes the best use of it.

Through thermal wind considerations the temperature field was tested to see if it supported the amount of vertical wind shear that existed in the u field. Individual point values did not show geostrophic agreement but above 725 mb the amount of temperature change, averaged in y, required by the wind shear was comparable to the observed temperature change across the domain, thus indicating geostrophic agreement over the domain as a whole. But, on the average, between 875 and 725 mb the wind shear

required a temperature drop across the domain, while the observed temperatures increased. Of course, in lower layers geostrophic agreement is not expected because of the effects of surface friction, but here the disagreement could also be due to suspect analyses in the region of very little data.

The v component of the wind, relative to a moving frame of reference, is presented in Fig. 16. Positive v values indicate motion to the rear of the system. Along each pressure surface a maximum in v is present from 875 up to 725 mb at -10 min. Note that this maximum is at the right edge of the most intense radar echoes, similar to the case of S & P. Strong convergence is noticeable from 0 to +40 min between 900 and 750 mb and between 550 and 450 mb. The west-northwesterly flow above 800 mb after +30 min is noticeable in the tilt of the balloon trajectories shown in Fig. 14.

Crude estimates of $\frac{\partial \theta}{\partial x}$ showed little systematic structure, leading us to conclude that the pattern of vertical shear in Fig. 16 is almost wholly ageostrophic.

b. divergence and vertical wind component

For each of the twelve pressure layers between 959 and 400 mb the divergence, D, was computed from

$$D_K = \left[\left(\frac{\partial u}{\partial x}\right)_p + \left(\frac{\partial v}{\partial y}\right)_p \right]_K ,$$

where u and v represent the average velocity component in the K layer (not x-averaged) and p denotes reference to constant-pressure surfaces. Note that here (only here) the derivative in the x direction is obtained by use of finite difference methods over an interval of 10 km and not by the method described in the Appendix. The distribution of divergence

was averaged in x for each pressure layer and the resulting distribution is shown in the y-p plane in Fig. 17.

Interesting features are the divergent-convergent doublet from -40 to +60 min below 600 mb and the convergent-divergent doublet from -40 to +80 min above 550 mb. The divergent cores are due to divergence in both the u and v fields. The convergent areas are due primarily to the strong convergence in v that was mentioned above.

To provide the divergence pattern at the surface, $\frac{\partial u}{\partial x}$ and $\frac{\partial v}{\partial y}$ were determined from 10-min averages of winds measured by surface stations of the network. Isopleths of u and v were drawn and from these the magnitudes of $\frac{\partial u}{\partial x}$ and $\frac{\partial v}{\partial y}$ were determined over an interval of 8 km in both the x and y directions. The surface divergence pattern for 1640 CST is shown in Fig. 18. Convergence on the order of 10^{-3} sec^{-1} is occurring some 10 to 20 min ahead of the LERE and 10 to 20 min behind the actual leading edge of radar echoes. Judging from pre-LERE soundings this is a sufficient amount of convergence to provide the necessary lift to release the potential instability and trigger convective activity over a matter of minutes. The divergence behind the 1640 CST LERE line is probably due to downdraft from decaying radar cells.

The kinematic method of computing vertical velocities consists of computing the divergence directly from the observed winds. When the divergence has been computed stepwise integration of the continuity equation

$$\frac{\partial \omega}{\partial p} + D_K = 0 \qquad (1)$$

yields the vertical component of velocity, ω, at the top of all K layers:

$$\omega(x,y,p_K - \tfrac{1}{2}\Delta p) = \omega(x,y,p_{sfc}) + \sum_{1}^{K} D_K \Delta p \qquad (2)$$

where Δp = 9 mb for K = 1 and 50 mb for all other K, and $\omega(x, y, p_{sfc})$, the vertical motion at the surface, is ignored in the calculation since the ω's computed aloft are much greater.

Now Fankhauser (1969) contends that the vertical velocity computed from the kinematic technique produces reasonable values at low and middle levels but diminishes in credibility in the upper layers. He attributes the decrease with height in the reliability of kinematic vertical motion estimates to at least two facts. First, the quality of wind measurements from a GMD-1 system (the type used at NSSL) deteriorates with decreasing elevation angles, due to the combined consequence of strong uniform winds aloft and sounding duration. Second, as a result of integrating (1), errors in the wind analysis in individual layers tend to accumulate with height. He suggests a scheme for the correction of this problem which includes the assumption that ω approaches zero at 100 mb.

In an effort to test the reliability of kinematically determined vertical motions, $\tilde{\omega}$, the average vertical motion over the domain from -53.0 to +47.7 km was computed by the approximation

$$\tilde{\omega}\,(p) = \int_{p}^{P_{sfc}} \left\{ \frac{v_{+47.7}(p) - v_{-53.0}(p)}{100.7 \text{ km}} + \overline{\frac{\partial u}{\partial x}} \right\} dp \quad ,$$

where $\overline{\frac{\partial u}{\partial x}}$ is the average $\frac{\partial u}{\partial x}$ for each y for each pressure level. The result of this computation is shown in Fig. 19.

Ascent reaches a maximum at 400 mb, the upper limit of the data. Above this level it is not known if the profile will approach zero at 100 mb, so we cannot disprove Fankhauser's (1969) contention. However, since his results (see his Fig. 12) showed that significant adjustments

in the vertical motions were only necessary above 400 mb and since the kinematically determined vertical motions of S & P were reasonable, we are confident that our kinematically determined ω's do not suffer greatly from errors due to spurious divergences over deep layers.

The profile in Fig. 19 reveals an irregularity near 750 mb as in the case of S & P. The occurrence of this irregularity in both cases is probably incidental. Fig. 17 shows that the first impetus to upward vertical motion below 800 mb is due to strong convergence over a large region. Above 650 mb the upward motion is given a second push by strong convergence aloft. This entire portion of the updraft is believed to be a result of condensational heating due to mesoscale ascent of saturated air triggered by the surface convergence discussed above, as in S & P.

The vertical motion pattern, presented in Fig. 20, was calculated from (2) at the top of all K layers and then averaged in x. The most prominent feature is the downdraft-updraft doublet between - 50 and +60 min, the downdraft being centered at -20 min and the updraft centered at +10 min. S & P also found this same kind of doublet pattern in their examination of a frontal disturbance. Their region of descent was somewhat wider and the peak descent, which was somewhat stronger, occurred near 400 mb. An alternative analysis which was performed later on their data reduced the magnitude of this descent by one-half, but it was still about 40×10^{-3} mb sec^{-1} stronger than the peak descent shown in Fig. 20. The occurrence of this downdraft-updraft doublet in two cases that were of entirely different synoptic origin led to the search for other cases which exhibited the same kind of mesoscale circulation pattern.

Fankhauser's (1974) vertical motions, obtained in his analysis of a squall-line case, also showed a downdraft-updraft doublet. The peak

upward and downward motions were somewhat weaker than the ones shown here. On the basis of the results from these three cases one can tentatively conclude that this type of mesoscale circulation exists in the presence of severe storms during their mature stages whether they be of frontal or squall-line character.

From the v field shown in Fig. 16 and the kinematically calculated ω's a streamfunction was calculated for motions in the y-p plane by using the formulas,

$$\omega = \frac{\partial \Psi}{\partial y} \quad , \qquad v = - \frac{\partial \Psi}{\partial p} \quad .$$

Now Ψ cannot accurately represent the flow since $\frac{\partial u}{\partial x}$ is not zero, but it can portray either the ω or v field correctly everywhere. We have chosen to represent the actual ω's since we believe that the vertical transports following the mean mesoscale motions are the most important ones; this belief is supported in the budget calculations. The v's at -5.3 km were used as boundary conditions and Ψ was arbitrarily set equal to zero at 955 mb.

The streamfunction lines of flow are shown as the dashed lines in Fig. 21. It is important to note that the streamfunction lines in the lower layers do not show any upward motion between -20 and 0 min, where we believe low-level convergence is responsible for triggering the convective activity. Ascent is probably not visible because of the smoothing and averaging processes that have been applied to the available data.

c. mixing ratio

An analysis of the mixing ratio following the procedure outlined in the Appendix indicates relative humidities around 50 to 60% in the location of most intense and persistent radar echoes. This inconsistency is attributable to lack of soundings in this region, where the air must

be saturated or very nearly so. The analysis was adjusted in this region to be consistent with the radar echoes, by accepting the temperature analysis as correct and by changing the mixing ratio values so that the relative humidity in this region was 94%, a somewhat arbitrary value that corresponds to the average value of relative humidity over all the 29 surface recording stations. This value was taken as a lower limit of what might be expected aloft.

The resulting field of mixing ratio, q, is shown in Fig. 21. Note that this adjustment tends to make the horizontal gradients near -20 and near +45 min extremely strong. The strength of these gradients may be excessive and they might yield spuriously strong sources and sinks in the budget calculations. The tight vertical gradient before -20 min in the 850 to 750 mb layer is supported by individual soundings, especially those launched in the southwestern part of the network prior to the arrival of the LERE, which showed a moist layer from the surface up to about 800 mb abruptly capped by a dry layer, which extended up to about 600 mb, with another moist layer aloft. The analysis shows these features. Examination of individual soundings and surface observations indicates that the upper moist layer prior to -20 min represents a cloud deck of altocumulus, mainly in the southwestern part of the network.

As for relative humidity, one dry region is intruding from the right centered at 700 mb and another one is intruding from the left centered near 525 mb as shown in Fig. 21. The air is very moist near the surface over the whole domain.

In Fig. 21 the streamfunction lines are superimposed on the q distribution to provide a visual impression of the rate of change of q following the mean mesoscale motion in the y-p plane. In the flow through the system at lower levels prior to -40 min, q is on the average

conserved. Elsewhere q decreases in regions of ascent and increases in regions of descent (except in the region near the middle cloud deck where q decreases in a region of descent, which seems to be a spurious loss of moisture).

d. equivalent-potential temperature

The equivalent-potential temperature, θ_e, was calculated for each y at each pressure level using the formula

$$\theta_e = \theta \exp [(Lq) / (C_pT)] ,$$

where L is the latent heat of condensation, c_p is the specific heat of air at constant pressure, and T is the temperature. The values of θ and q shown in Figs. 21 and 23 were used in this calculation. The θ_e distribution appears in Fig. 22. The horizontal gradients near -20 and +40 min may be too strong because of the adjustment made in the mixing ratio field. Prior to -15 min θ_e decreases from 900 mb up to a minimum near 725 mb, indicating potential instability in this layer. Above there θ_e increases upward until a maximum is reached near 575 mb, followed again by a decrease in θ_e up to 450 mb.

In the principal mesoscale updraft region above 800 mb θ_e decreases upward to a minimum near 475 mb above which it increases. This minimum may not really be as high as presented. The adjustment in q tended to make the level of the minimum higher.

A qualitative look at the changes in θ_e following the mean mesoscale motion in the y-p plane shows θ_e is not conserved in most places. Some features are physically impossible to explain on the basis of this two-dimensional flow; the u component must also be considered. Some probably cannot be explained even then. These features are discussed in detail in the section on budget calculations.

e. potential temperature

The field of potential temperature, θ, appears in Fig. 23. In the lower layers up to 850 mb before -20 min the potential temperature distribution is nearly horizontal. After -70 min between 750 and 550 mb the analysis shows a general cooling toward the west-northwest.

In general as the air moves through the system it is heated, however for the air entering from the west-northwest at about 500 mb the value of θ at its entrance is higher than the value at its exist.

6. Mesoscale budgets

a. discussion of concepts

The main objective of this study is to determine the importance of convection upon the heat, moisture, and momentum structure of the mean mesoscale atmosphere. These effects can be estimated as residuals in budgets in which the transports by the mesoscale motions are explicitly calculated. The approach to this problem is the same as that of S & P. The budget is considered for a quantity Q in a mesoscale volume 50 mb deep, 10.6 km in the y direction, and 30 km in the x direction. The overbar is used to indicate an average over such a volume and the prime is used to indicate deviations from this average value. The meteorological variables presented in the previous section are synonymous with the corresponding barred quantities presented in this section. We have:

$$\bar{\dot{Q}} = \frac{\partial \bar{Q}}{\partial t} + \frac{\partial}{\partial x}(\bar{U}\bar{Q}) + \frac{\partial}{\partial y}(\bar{V}\bar{Q}) + \frac{\partial}{\partial p}(\bar{\omega}\bar{Q}) + \frac{\partial}{\partial x}(\overline{U'Q'}) + \frac{\partial}{\partial y}(\overline{V'Q'}) + \frac{\partial}{\partial p}(\overline{\omega'Q'}) \tag{3}$$

where $\bar{\dot{Q}}$ is the real source. The apparent source is denoted by

$$\dot{Q}^{*} \equiv \frac{\partial \bar{Q}}{\partial t} + \frac{\partial}{\partial x}(\bar{U}\bar{Q}) + \frac{\partial}{\partial y}(\bar{V}\bar{Q}) + \frac{\partial}{\partial p}(\bar{\omega}\bar{Q}), \tag{4}$$

the rate of change following the mesoscale motion. A virtual source, denoted by

$$\dot{Q}^{v} \equiv -\left[\frac{\partial}{\partial x}(\overline{U'Q'}) + \frac{\partial}{\partial y}(\overline{V'Q'}) + \frac{\partial}{\partial p}(\overline{\omega'Q'})\right], \tag{5}$$

is assumed to essentially represent the effects of convective elements, except in the surface boundary layer where the effects of surface friction are included. Rewriting (3) using (4) and (5)

$$\dot{Q}^{*} = \bar{\dot{Q}} + \dot{Q}^{v}.$$

From the analysis of the mesoscale mean fields all the terms of $\dot{Q}^*$ can be calculated except for $\frac{\partial \bar{Q}}{\partial t}$. We shall denote $\dot{Q}^*$ minus $\frac{\partial \bar{Q}}{\partial t}$ as $\dot{Q}^{**}$ and refer to it as the approximate apparent source. The virtual source and $\frac{\partial \bar{Q}}{\partial t}$ can be determined only as residuals.

b. equivalent-potential temperature

The approximate apparent source of $\bar{\theta}_e$ is displayed in Fig. 24a. Assuming adiabatic processes $\dot{\theta}_e^* = \dot{\theta}_e^v$. Hence the apparent source of $\bar{\theta}_e$ is due entirely to the virtual source, which is presumably associated with convection.

In Fig. 24a, the large source region just prior to the LERE between 850 and 750 mb can perhaps be accounted for as a result of convective elements transferring high $\bar{\theta}_e$ from near the surface into this region. But the magnitude of the corresponding sink is no more than .2 deg K min^{-1}, while the source is as high as .8 deg K min^{-1}. Part of this discrepancy is due to the spurious source which was introduced when the mixing ratio field was adjusted. If $\bar{\theta}_e$ were reduced at lower levels near 0 min the apparent sink would be larger.

The large sink near -20 min centered at 650 mb is physically impossible to explain on the basis of convection. Its location is just above a stable layer shown in the $\bar{\theta}_e$ field in Fig. 22. A slight modification in the $\bar{\theta}_e$ and Ψ analysis making the contours parallel to the streamlines in this region would eliminate part of this sink. Also a large part of this loss is due to the change in $\bar{\theta}_e$ in the x direction.

Suppose that the local changes in the moving coordinate system are just those produced by the $\bar{u}$ transport. Then the apparent rates of change are due entirely to the $\bar{v}$ and $\bar{\omega}$ transports. The sum of these two terms, for $\bar{\theta}_e$, is shown in Fig. 24b. The sink centered at -20 min

discussed above has been greatly reduced. In both presentations convective elements are transferring high values of $\bar{\theta}_e$ from below 475 mb to above this level in the region of most intense radar echoes.

c. potential temperature

In Fig. 25a is the approximate apparent source of $\bar{\theta}$. Apparent heating and cooling are primarily taking place in regions of mesoscale ascent and descent, respectively. Before -10 min in the layer between 850 and 750 mb there is an apparent sink of $\bar{\theta}$ and source of $\bar{\theta}_e$. It is believed to be in this region that the initial cumulus convective clouds, triggered by low-level convergence, were evaporating into the dry air above 800 mb, thus accounting for the cooling here. Above 650 mb the cooling is probably due to evaporation of the middle cloud deck entering the southwestern part of the network. These regions of cooling appear to be driving the mesoscale downdraft.

In the main updraft region, where the air is nearly saturated on the mesoscale, the apparent source is essentially a real source, latent heat of condensation. The effect of convection here is probably to elevate the level of maximum heating.

Changes are on the order of .1 deg K min^{-1} over much of the system with peak heating of .5 deg K min^{-1} and peak cooling of .3 deg K min^{-1}. Exclusion of the $\bar{u}$ transport does not change the field much. A comparison of Figs. 25a and 25b shows that $\frac{\partial}{\partial x}(\bar{u}\ \bar{\theta})$ is not significant.

d. mixing ratio

The approximate apparent source of $\bar{q}$ is presented in Fig. 26a. The source at -20 min centered near 800 mb is due to evaporation of cumulus convective clouds, which were initially set off by low-level convergence, into the dry air in middle levels. The strength of this source

may be somewhat exaggerated, because of reasons mentioned earlier. It is accompanied by a much weaker sink below it. The source above 600 mb near -20 min is due to evaporation of the cloud deck entering the southwestern part of the network.

The large loss of $\bar{q}$ in the region of mesoscale ascent between 0 and +60 min is due primarily to condensation. It's not clear here what the effect of convection is. The apparent loss between 700 and 600 mb just prior to -20 min is not readily explained. Part of it is due to the $\bar{u}$ transport of $\bar{q}$, which may be balanced by the local change of $\bar{q}$. In Fig. 26b is the approximate apparent source of $\bar{q}$ less the $\bar{u}$ transport. The moisture loss between 700 and 600 mb before -20 min has been reduced by one-half and the distribution is physically more pleasing.

The rainfall rate relative to the LERE appears in Fig. 27. Rain at the surface coincides the mesoscale updraft region. The maximum rate occurs at +20 min some 10 min after peak ascent is reached in this region.

e. $\bar{v}$ - momentum

The equation of motion in the y direction can be written as

$$\frac{\partial \bar{v}}{\partial t} + \bar{u}\frac{\partial \bar{v}}{\partial x} + \bar{v}\frac{\partial \bar{v}}{\partial y} + \bar{\omega}\frac{\partial \bar{v}}{\partial p} = -\frac{\partial \Phi}{\partial y} - f\bar{u} - \left[\frac{\partial}{\partial x}(\overline{u^1v^1}) + \frac{\partial}{\partial y}(\overline{v^1v^1}) + \frac{\partial}{\partial p}(\overline{\omega^1v^1})\right] \quad (6)$$

where Φ is the geopotential on a constant-pressure surface. The sum of the terms on the left hand side of (6) represent the acceleration following the mean mesoscale motion. We shall refer to the sum of the last three terms on the left as the approximate mesoscale acceleration. The first and second terms on the right hand side of (6) represent the pressure gradient and coriolis forces, respectively. The last three terms on the right represent forces arising from surface friction and from internal

turbulent stresses (primarily convective).

The coriolis force and the approximate mesoscale acceleration were determined from the mesoscale analysis. The surface friction force was parameterized in the lowest layer as

$$- C_d H^{-1} \bar{V}(\bar{U}^2 + \bar{V}^2)^{\frac{1}{2}} ,$$

where C_d is a drag coefficient of 2×10^{-3}, H is a layer of 200 meters, and $\bar{v}$ was taken relative to the ground.

In Fig. 28 is the analysis of the coriolis force over the whole domain and the parameterized surface friction force in the lowest layer. Note that the coriolis force is considerable and always acts toward the east-southeast. In the lowest layer prior to +60 min the surface friction and coriolis forces combine to act against the east-southeasterly flow.

Shown in Fig. 29 are the approximate mesoscale accelerations. Below 800 mb mesoscale accelerations are generally west-northwestward before -10 min and east-southeastward after. Figure 28 indicates that the coriolis force is responsible for some of this east-southeastward acceleration. Above 500 mb between -10 and +50 min strong accelerations toward the west-northwest are present, despite opposing coriolis forces here. These strong accelerations are due primarily to the rather abrupt increase of $\bar{v}$ upwards, which was evident in individual soundings.

7. Concluding remarks

This study has examined the case of the 26 April 1969 squall line which moved ahead of a surface cold front through the NSSL mesonetwork in Oklahoma.

The squall-line system was within the NSSL mesonetwork about 2 hours and produced rain amounts up to 1.25 inches at some stations. Hail with 1.75-inch diameter was recorded at one station in the southern part of the network, and just outside NSSL the system spawned a tornado which caused considerable damage. This system can be regarded as severe.

It seems that the squall-line thunderstorms did not appear spontaneously in the warm air ahead of the front but first appeared behind it, formed a uniform line, and then moved out ahead of the front. Since the cold front moves with a speed close to that of the low-level winds, and the air near the squall line derives its momentum from higher levels, where stronger winds prevail, it follows that the squall line must move at a rate faster than the surface cold front.

Although the analysis of the squall-line system was presented in a two-dimensional display transverse to the leading edge of the radar echoes to permit maximum use of the available data, the three-dimensional characteristics of the system were evident in the surface and rawinsonde observations. The surface wind shift and temperature break associated with the gust front revealed a curved-shaped pattern with the two events arriving in the northern part of the network after the onset of precipitation. Strong southwesterly flow did not justify the assumption of small variations along the leading edge of the radar echo line, so crude estimates of these variations had to be made.

Despite the three-dimensional structure of the system, the two

dimensional display gave some interesting results. The mechanism of the system appears to work as follows: surface convergence (due to the gust front) of the order of 10^{-3} sec^{-1} first triggers convective activity. An intense mesoscale downdraft-updraft doublet develops, the downdraft being centered about 10 km behind the leading edge of the radar echoes and the updraft centered about 5 km ahead of it. Peak speeds in the downdraft reach about 1.3 m sec^{-1} at 550 mb, while peak speeds in the updraft reach about 2.5 m sec^{-1} at 400 mb. These vertical currents appear to be driven by a corresponding doublet of cooling and heating with peak rates of .3 deg K per min of cooling and .5 deg K per min of heating. The cooling is produced by evaporation of initial convective cloud tops in the dry air in middle layers and from the dissipation of a middle cloud layer, and the heating is produced by latent heat release due to condensation of water vapor along with the superimposed convection.

This downdraft-updraft doublet is not only characteristic of this case but of cases studied by Fankhauser (1974) and Sanders and Paine (1975). The synoptic situation was not the same in all three cases. Two cases were squall-lines, while the convection resulted from frontal over-running in the other. On the basis of these studies it is tentatively concluded that this doublet of mesoscale vertical motions may be a distinguishing feature of large convective storm systems in their mature stages, whether they be of frontal or squall-line character.

The lack of data prevented the complete analysis of the effect of convective activity on the mean mesoscale atmosphere. However convection plays an important role in providing the liquid water for evaporation and supplying some of the heating needed to drive the updraft and cooling for the downdraft.

Future studies of this kind will require more soundings, both in and out of storm areas. Although Barnes (1974) suggests that no economically feasible combination of rawinsondes will ever completely resolve flow patterns and thermodynamic structure within severe storms, rawinsondes are still the most reliable system for providing simultaneous wind data at many vertical levels. The dual-Doppler radar systems can also be used to realize internal flow.

ACKNOWLEDGEMENTS

I am deeply indebted to Professor Frederick Sanders for introducing me to the 26 April 1969 case, offering assistance and helpful discussions throughout this research work, and spending time examining the rough draft of this paper. Thanks are extended to David Katz and Razia Ahmad for their assistance in the initial preparation and analysis of the data, Isabelle Kole for drafting the figures, and Virginia Mills for typing the final draft. Special thanks are due to my parents and friends for their love and support.

APPENDIX

Fig. 13 shows the coordinate system used to process the rawinsonde data. The x axis is aligned with the mean LERE line and is assumed to point 27 deg to the right of true north. The positive y axis points toward the rear of the system and passes through surface station 5E. The origin of the system is assumed to lie on the mean LERE line and to move with a velocity, $\underset{\sim}{v} = -.53\hat{j}$ km min^{-1}, $\hat{j}$ being the unit vector in the y direction. The t coordinate is defined to be coincident with the y coordinate, by the relation t = y/.53. Positive t values are defined as the time since the LERE line passed the point located at y.

In order to determine the x, y, and t coordinates of the balloons at each pressure level the position of each of the 23 soundings was plotted from its point of release up to 425 mb. The t coordinate of the balloon at any pressure level was determined by

$$t(p) = t_R + t_E - t_{LERE} ,$$

where t_R is the release time of the balloon, t_E is the elapsed time since release of the balloon, and t_{LERE} is the time the LERE line passed the position of the balloon. The y coordinate was determined by use of $y = .53\ t(p)$. The x coordinate was determined by measuring the distance of the balloon from the y axis along a line parallel to the x axis.

Once the positions of the balloons were known for each pressure layer the meteorological variables associated with these positions were plotted in the x-y plane for the twelve pressure levels between 959 and 400 mb. These horizontal charts were analyzed objectively and 286 data points were determined for a rectangular area, with x ranging between -20 and +40 km and y ranging between -58.3 and +53.0 km (t ranging between -110 and +100 min). The variables were then averaged in x to

give a y-p display of the significant meteorological variables.

Derivatives in the y and p directions were obtained by use of finite difference methods. The pressure interval is 50 mb while the interval in the y direction is 10.6 km (or 20 min). Derivatives of any quantity in the x direction were obtained by dividing the rectangular grid in half by a line parallel to the y axis, averaging the quantity in x in each half of the grid for each y, assigning this average value to the midpoint in each half section, and then using finite difference methods over an interval of 30 km. Unfortunately sparsity of data prevented the measurement of local changes.

REFERENCES

Barnes, S. L., 1974: Papers on Oklahoma thunderstorms, April 29-30, 1970. NOAA TM ERL NSSL-69.

_____, J. H. Henderson, and R. J. Ketchum, 1971: Rawinsonde observation and processing techniques at the National Severe Storms Laboratory. NOAA TM ERL NSSL-53.

Browning, K. A., 1964: Airflow and precipitation trajectories within severe local storms which travel to the right of the winds. J. Atmos. Sci., 21, 634-639.

Byers, H. R., 1974: General Meteorology. New York: McGraw-Hill Book Co., 300-304.

Davies-Jones, R. and E. Kessler, 1974: Tornadoes. Offprint from: Weather and Climate Modification. Dr. Wilmet N. Hess, editor. New York: John Wiley & Sons, Inc., 552-595.

Fankhauser, J. C., 1969: Convective processes resolved by a mesoscale rawinsonde network. J. Appl. Meteor., 8, 778-798.

_____, 1974: The derivation of consistent fields of wind and geopotential height from mesoscale rawinsonde data. J. Appl. Meteor., 13, 637-646.

Fawbush, E. J., R. C. Miller, and L. G. Starrett, 1951: An empirical method of forecasting tornado development. Bull. Amer. Meteor. Soc., 32, 1-9.

Lewis, J. M., Y. Ogura, and L. Gidel, 1974: Large-scale influences upon the generation of a mesoscale disturbance. Mon. Wea. Rev., 102, 545-560.

Newton, C. W., 1950: Structure and mechanism of the prefrontal squall line. J. Meteor., 7, 210-222.

_____, 1963: Dynamics of severe convective storms. Meteor. Monogr., 5, No. 27, 33-58.

Ogura, Y., and H. -R. Cho, 1973: Diagnostic determination of cumulus cloud populations from observed large-scale variables. J. Atmos. Sci., 30, 1276-1286.

Sanders, F., and R. J. Paine, 1975: The structure and thermodynamics of intense mesoscale convective storm in Oklahoma. J. Atmos. Sci., 32, 1563-1579.

U.S. Department of Commerce, 1969: Storm Data, 11, 33.

Yanai, M., S. Esbensen, and J. -H. Chu, 1973: Determination of bulk properties of tropical cloud clusters from large-scale heat and moisture budgets. J. Atmos. Sci., 30, 611-627.

Zittel, D., 1976: National Severe Storms Laboratory, Personal communication.

TABLE 1. WSR-57 Video Contour Levels and Equivalent Reflectivities

Level	Log Z_e	Shading	Code
1	2.04	Light Gray	2
2	3.20	Bright	3
3	4.23	Dark	4
4	5.18	Light Gray	5
5	6.20	Bright	6

FIGURE LEGENDS

Fig. 1 The 1969 NSSL upper-air and surface mesonetwork.

Fig. 2 Synoptic situation at 0600 CST, 26 April 1969. Boxed area indicates location of NSSL mesonetwork.

(a) Surface map. Solid lines are isobars (mb) of sea-level pressure; dashed lines are surface isotherms (^{o}C). Front, wind, cloud amount, and present weather phenomena are indicated in standard synoptic notation.

(b) 400 mb chart. Solid lines are height contours (decameters). Winds are indicated in standard synoptic notation.

Fig. 3 Tinker Air Force Base temperature and dew-point soundings on 26 April 1969. Winds are indicated in standard synoptic notation, north pointing to top of diagram.

(a) Soundings at 0600 CST

(b) Soundings at 1800 CST

Fig. 4 Same as Fig. 2a but for 0600 CST, 27 April 1969. Instability line indicated by heavy dash-dotted line.

Fig. 5 Surface maps over the state of Oklahoma on 26 April 1969 at (a) 0900, (b) 1200, (c) 1500, and (d) 1800 CST. Dashed-boxed area indicates location of NSSL mesonetwork. Solid lines are isobars (mb) of sea-level pressure. Front, wind, cloud amount, present weather phenomena, and instability line are indicated in standard synoptic-scale notation. Temperatures are given in deg F.

Fig. 6 Radar PPI presentations at three-hour intervals on 26 April 1969. Labelled solid lines represent coded values of log Z_e, the radar reflectivity factor at 0 deg elevation (see Table 1). Area enclosed by dashed lines is NSSL mesonetwork. Straight solid line is the average position of surface cold front. Tick marks indicate portions of the echoes that have entered the ground clutter of the radar.

(a) PPI presentation at 0900 CST

(b) PPI presentation at 1200 CST

(c) PPI presentation at 1500 CST

(d) PPI presentation at 1800 CST

Fig. 7 Temperature (^{o}F) and rainfall (inches) traces recorded at automatic surface recording station, 2C.

Fig. 8 Isochrones of first temperature break are solid lines. Isochrones of leading edge of radar echoes are dashed lines. Dash-dotted parts of dashed lines represent portions of the lines that have entered the ground clutter of the radar. Dots and x's represent stations of mesonetwork as shown in Fig. 1. All times CST.

Fig. 9 Isochrones (CST) of first westerly component in wind direction. Dots and x's as in Fig. 1.

Fig. 10 Isochrones (CST) of onset of rain. Dots and x's are as in Fig. 1.

Fig. 11 Isohyets of total amount of rainfall (inches) on 26 April 1969. Dots and x's are as in Fig. 1.

Fig. 12 Radar PPI presentations at half-hour intervals on 26 April 1969. Labelled solid lines, area enclosed by dashed lines, and tick marks are the same as in Fig. 6.

(a) PPI presentation at 1600 CST

(b) PPI presentation at 1630 CST

(c) PPI presentation at 1700 CST

Fig. 13 Isochrones (CST) of the LERE line (see text, section 4). Radar PPI presentation at 0 deg elevation at 1650 CST. Intensity levels 1 and 4 are shown. A coordinate system moving with the line is on the right. Area enclosed by dashed lines is as in Fig. 6.

Fig. 14 Projections of paths of the rawinsonde balloons in the y(t)-p plane. Dots represent positions of individual balloons at surface and 50-mb intervals. Dashed lines enclose radar echo region. Abscissor labelled in time and distance relative to the LERE line.

Fig. 15 u component of wind (m sec^{-1}) with respect to a fixed coordinate system. Positive values for air moving into the page.

Fig. 16 v component of wind (m sec^{-1}) with respect to a moving coordinate system. Positive values for air moving toward the left.

Fig. 17 Divergence of the horizontal wind field, labelled in units of 10^{-5} sec^{-1}.

Fig. 18 Surface divergence pattern at 1640 CST. Solid lines labelled in units of 10^{-4} sec^{-1}. Dashed lines are isochrones of the LERE line. The actual leading edge of radar echoes at 1640 CST is indicated by the thin solid line. Dots and x's are as in Fig. 1.

Fig. 19 Profile of domain-averaged vertical motion, $\tilde{\omega}(10^{-3}$ mb $\sec^{-1})$.

Fig. 20 Mesoscale vertical motions $\tilde{\omega}(10^{-3}$ mb $\sec^{-1})$ derived from conventional kinematic technique.

Fig. 21 Mesoscale mixing ratio, q' (g Kg^{-1}). Dashed lines are streamfunction lines of flow relative to the LERE line at intervals of 400 mb m $\sec^{-1}$. Hatching and stippling represent, respectively, areas of relative humidity less than 25% and greater than 75%.

Fig. 22 Mesoscale equivalent-potential temperature, θ_e(deg K). Streamfunction lines are as in Fig. 21.

Fig. 23 Mesoscale potential temperature, θ(deg K). Streamfunction lines are as in Fig. 21.

Fig. 24 (a) Approximate apparent source of equivalent-potential temperature, $\dot{\theta}_e^{**}$, labelled in units of 10^{-2} deg K $\min^{-1}$.

(b) Approximate apparent source of equivalent-potential temperature minus u transport, labelled in units of 10^{-2} deg K $\min^{-1}$.

Fig. 25 (a) Same as Fig. 24a except for potential temperature, $\dot{\theta}^{**}$.

(b) Same as Fig. 24b except for potential temperature.

Fig. 26 (a) Approximate apparent source of mixing ratio, $\dot{q}^{**}$, labelled in units 10^{-2} gm Kg^{-1} $\min^{-1}$.

(b) Approximate apparent source of mixing ratio minus $\bar{u}$ transport, labelled in units of 10^{-2} gm Kg^{-1} $\min^{-1}$.

Fig. 27 Measured surface rainfall rate in units of centimeters per 10 minutes.

Fig. 28 The coriolis force plus the parameterized surface friction force (in the lowest layer) per unit mass, labelled in units of 10^{-3} m $\sec^{-2}$.

Fig. 29 Approximate mesoscale $\bar{v}$-accelerations labelled in units of 10^{-3} m $\sec^{-2}$.

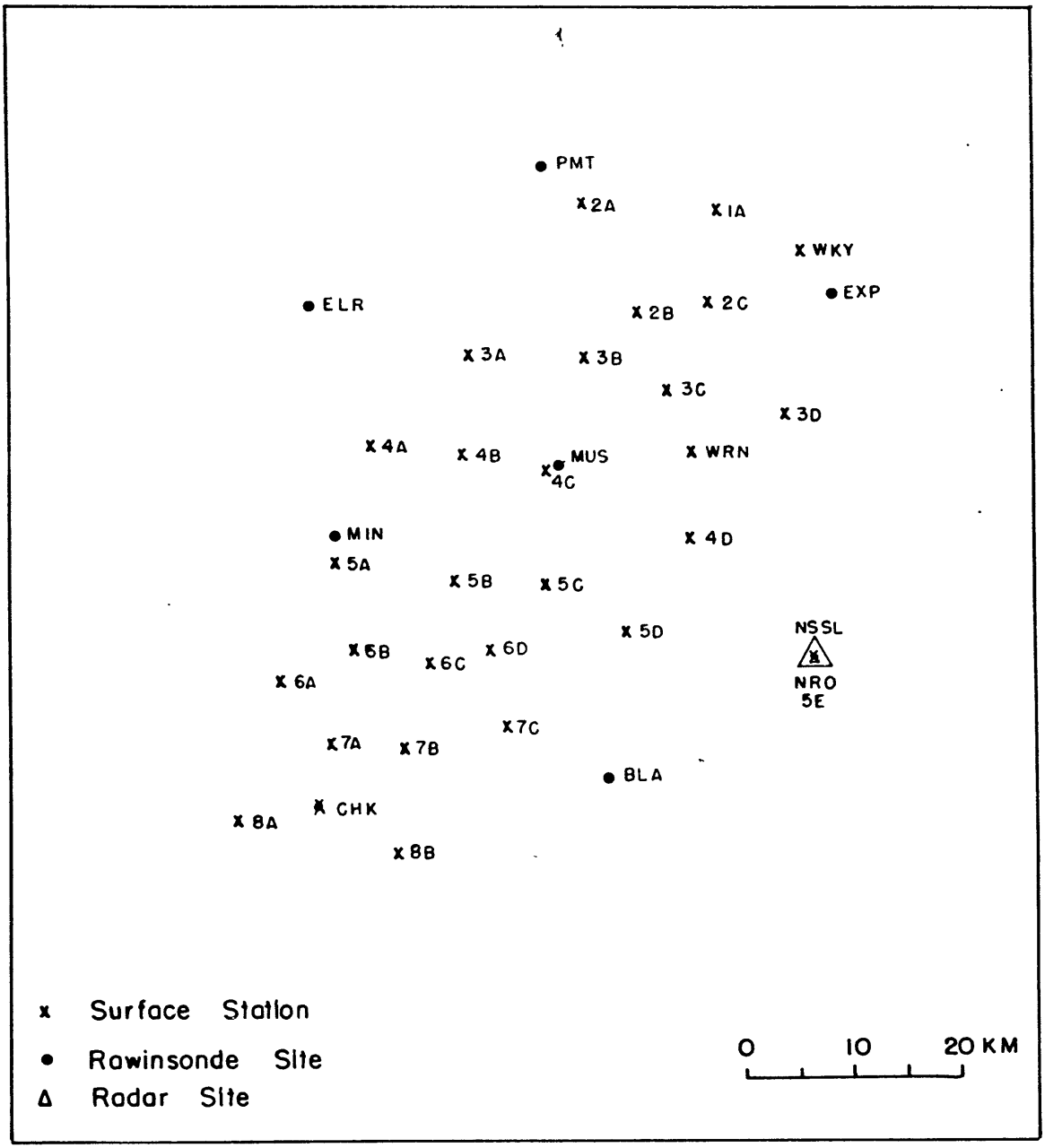
PMT
2A
1A
WKY
EXP
ELR
2B
2C
3A
3B
3C
3D
4A
4B
MUS
4C
WRN
MIN
4D
5A
5B
5C
5D
NSSL
6B
6C
6D
6A
NRO
5E
7C
7A
7B
BLA
CHK
8A
8B
Surface Station
Rawinsonde Site
Radar Site
0
10
20 KM

Fig. 1

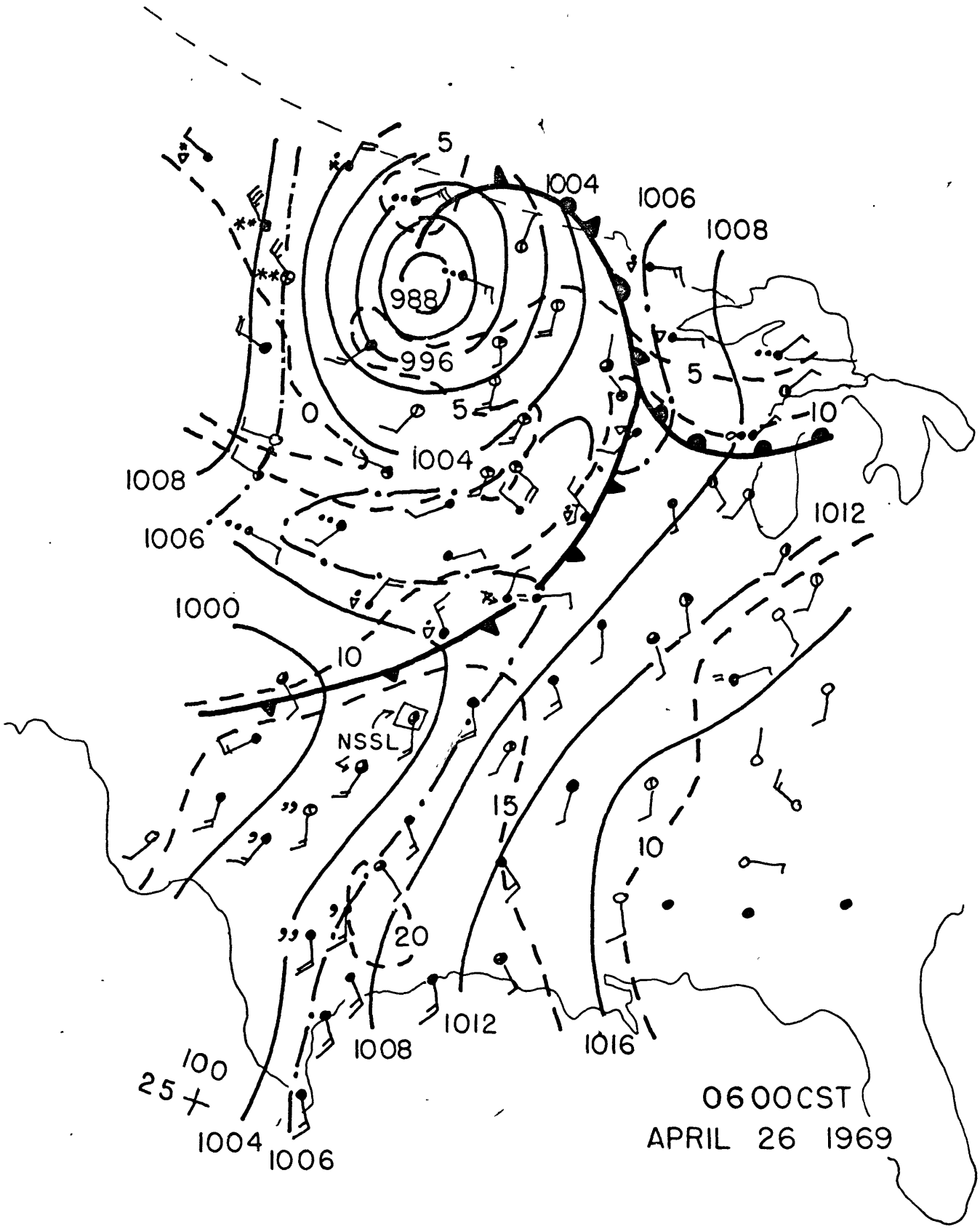
5
1004
1006
1008
988
996
5
0
5
10
1004
1008
1006
1012
1000
10
NSSL
15
10
20
1012
1008
1016
100
25
1004
1006
0600CST
APRIL 26 1969

Fig. 2a

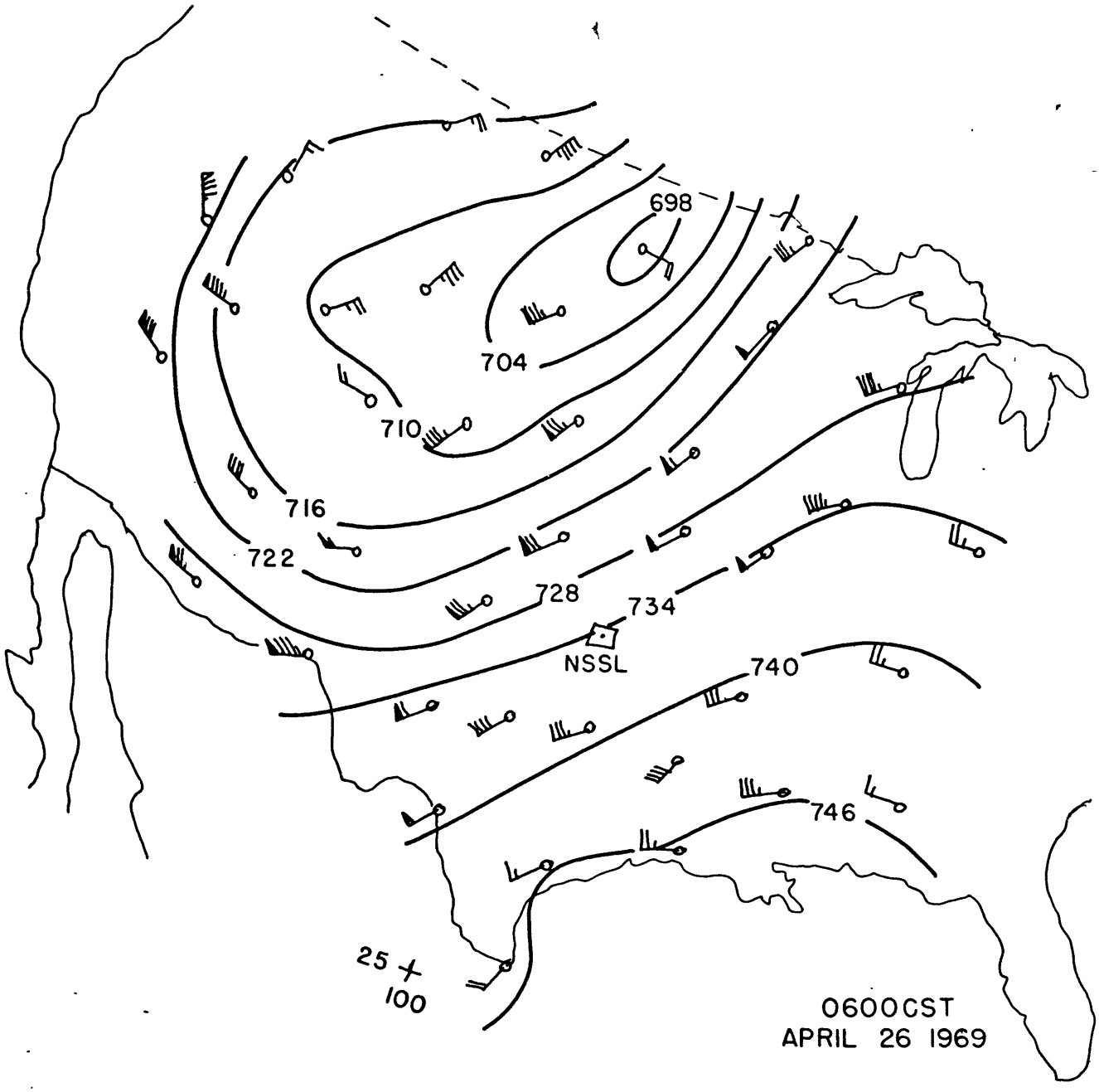
698
704
710
716
722
728
734
NSSL
740
746
25 x
100
0600CST
APRIL 26 1969

Fig. 2b

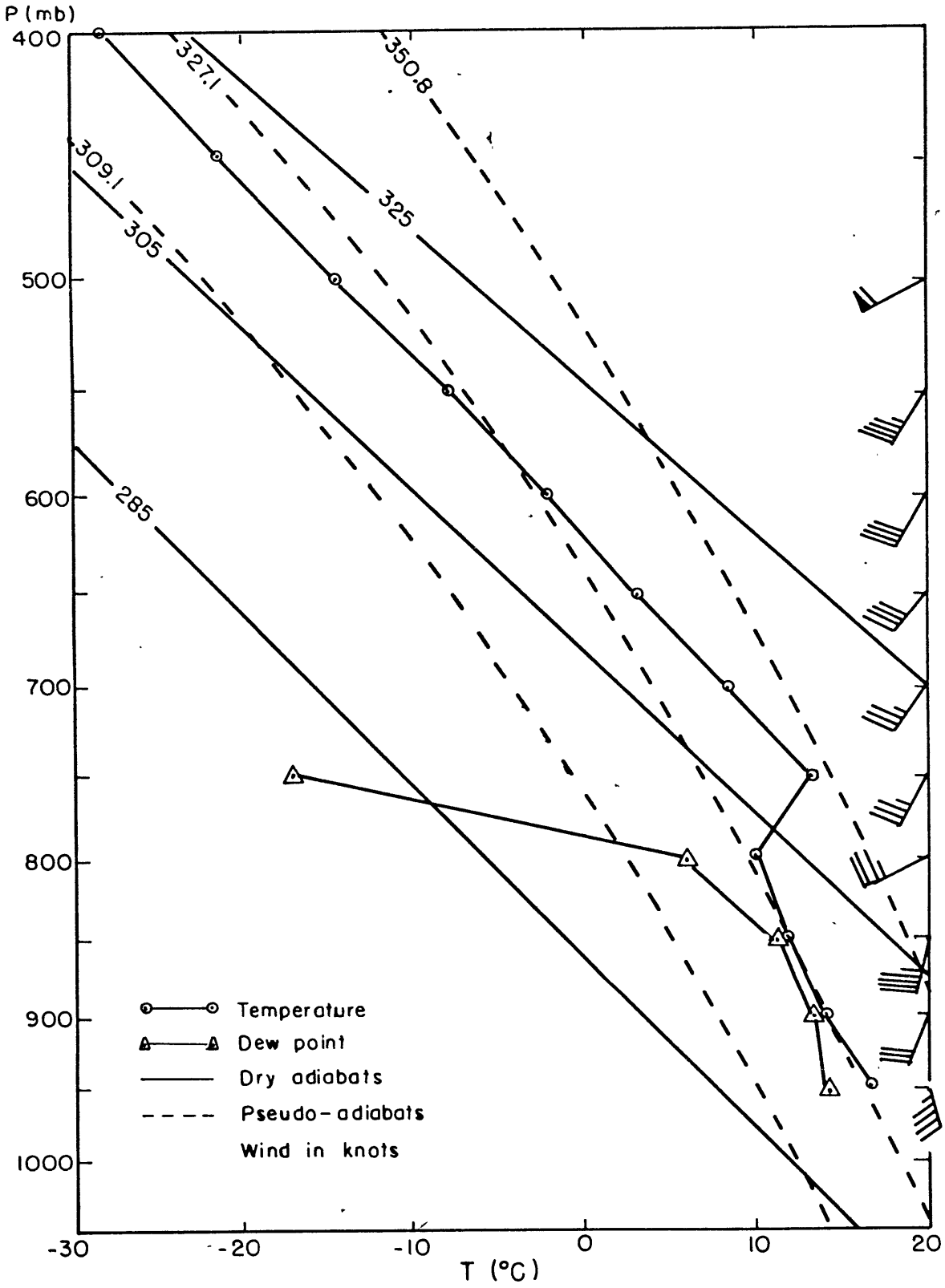
P (mb)
400
500
600
700
800
900
1000
-30
-20
-10
0
10
20
T (°C)
350.8
327.1
325
309.1
305
285
Temperature
Dew point
Dry adiabats
Pseudo-adiabats
Wind in knots

Fig. 3a

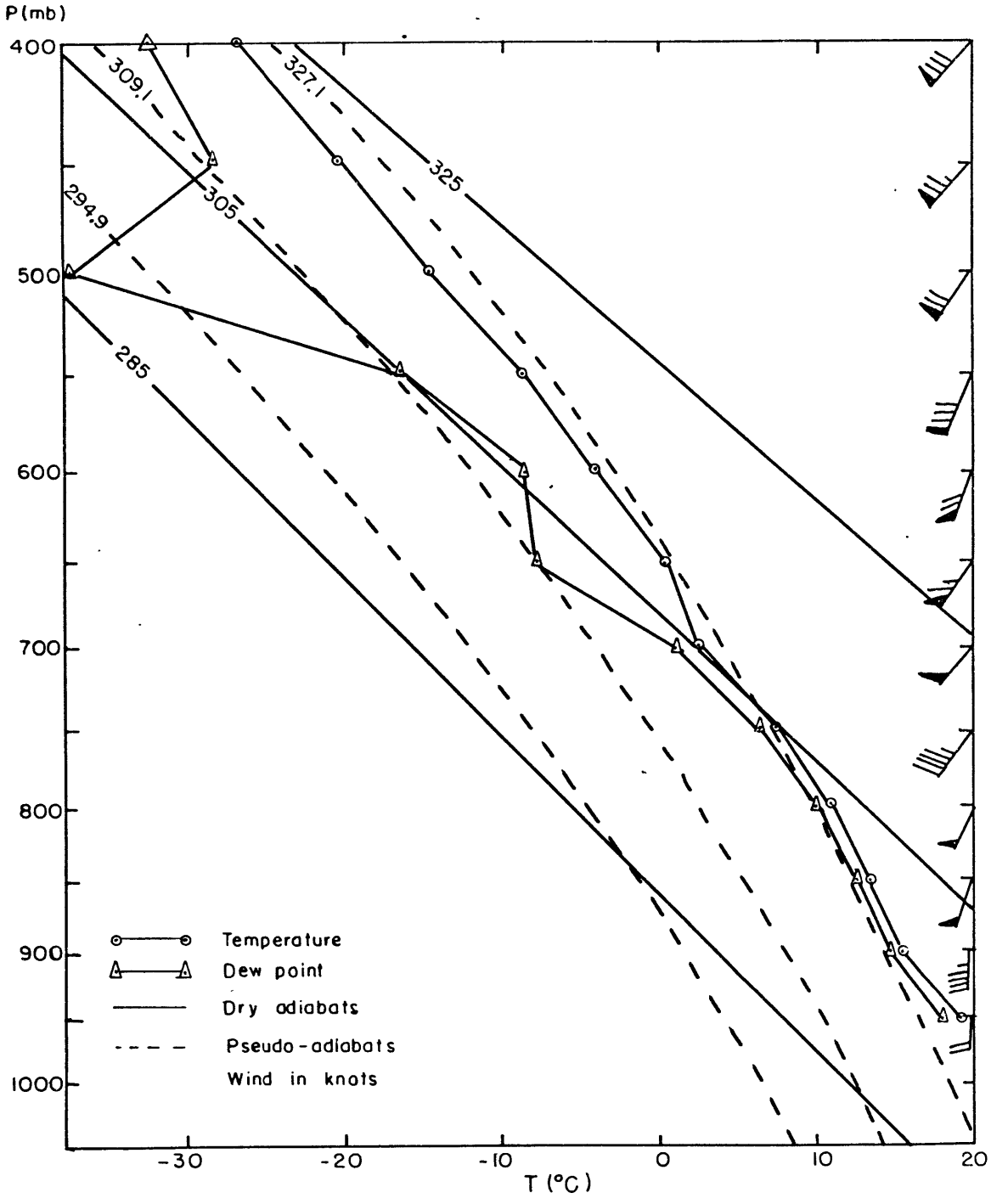
P(mb)
400
500
600
700
800
900
1000
309.1
327.1
325
305
294.9
285
Temperature
Dew point
Dry adiabats
Pseudo-adiabats
Wind in knots
-30
-20
-10
0
10
20
T (°C)

Fig. 3b

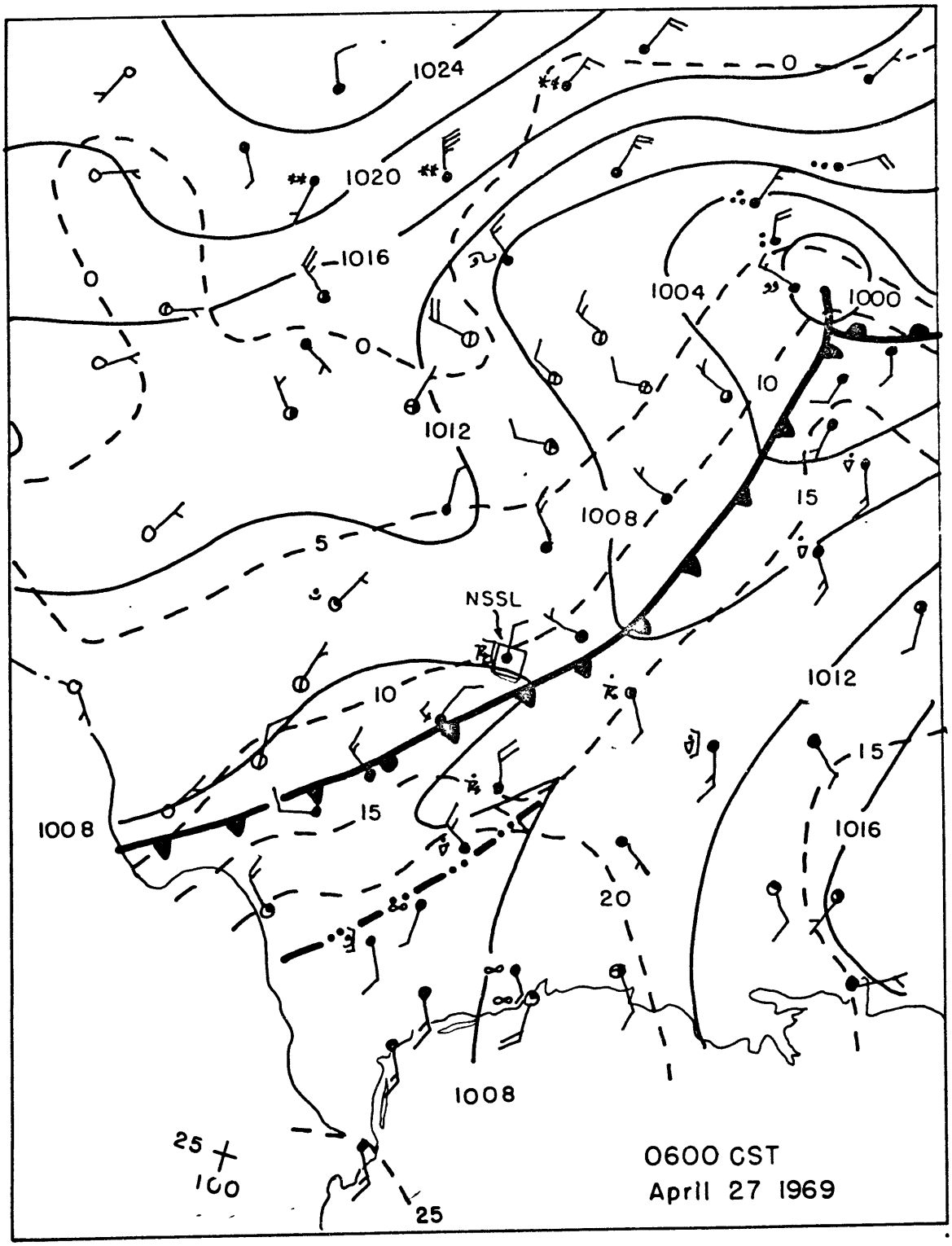
1024
1020
1016
1012
1008
1004
1000
0
5
10
15
20
25
NSSL
0600 CST
April 27 1969

Fig. 4

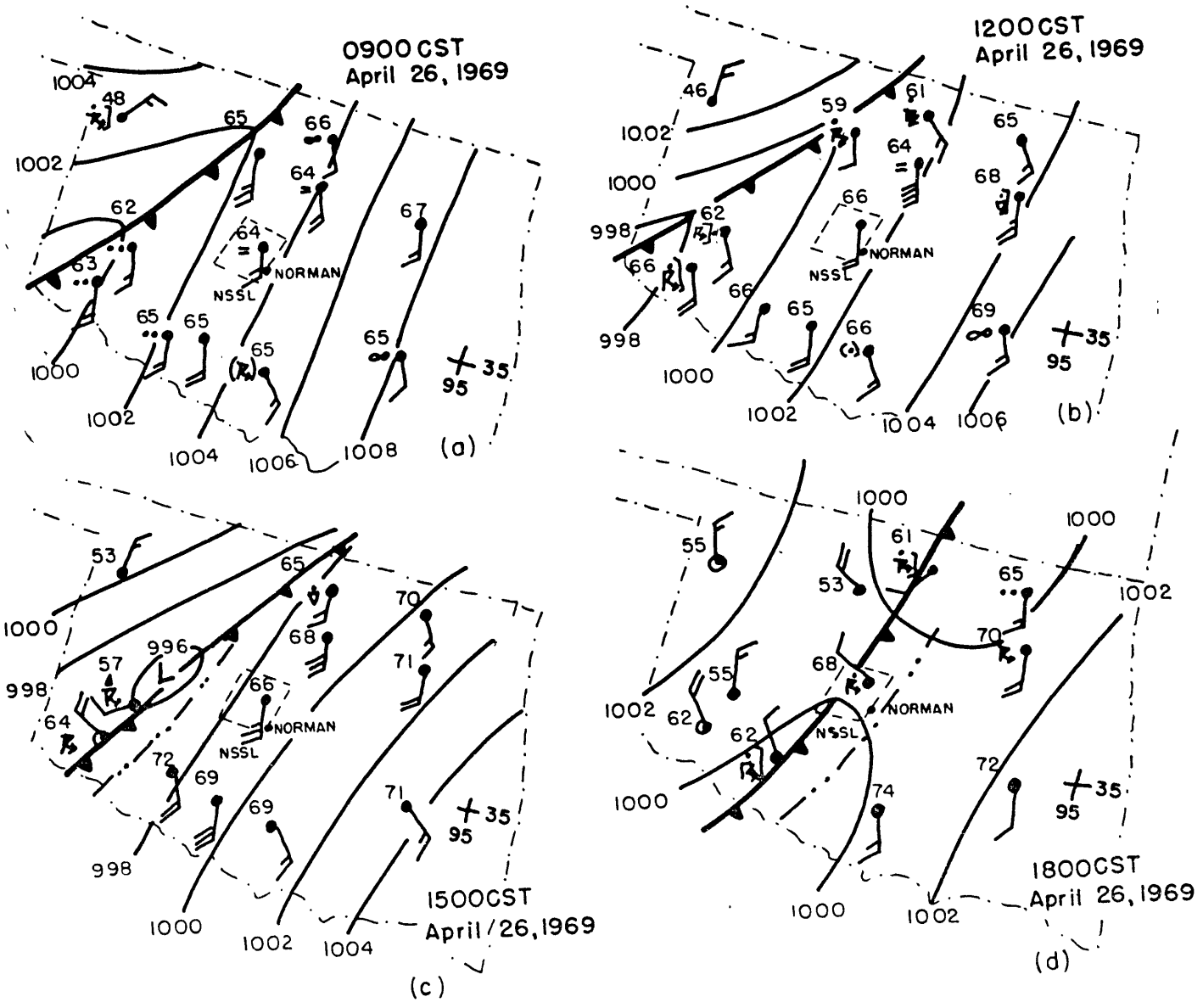
0900 CST
April 26, 1969
1004
48
65
66
1002
64
62
64
63
NSSL
NORMAN
67
65
65
65
1000
65
95
+35
1002
1004
1006
1008
(a)
1200 CST
April 26, 1969
46
59
61
1002
64
65
1000
66
68
62
998
66
NSSL
NORMAN
66
66
65
66
998
1000
69
95
+35
1002
1004
1006
(b)
53
65
1000
70
996
68
57
71
998
66
64
NORMAN
NSSL
72
69
69
71
95
+35
998
1000
1002
1004
1500 CST
April 26, 1969
(c)
1000
1000
55
61
53
65
1002
70
55
68
1002
62
NORMAN
62
NSSL
72
1000
74
95
+35
1000
1002
1800 CST
April 26, 1969
(d)

g. 5

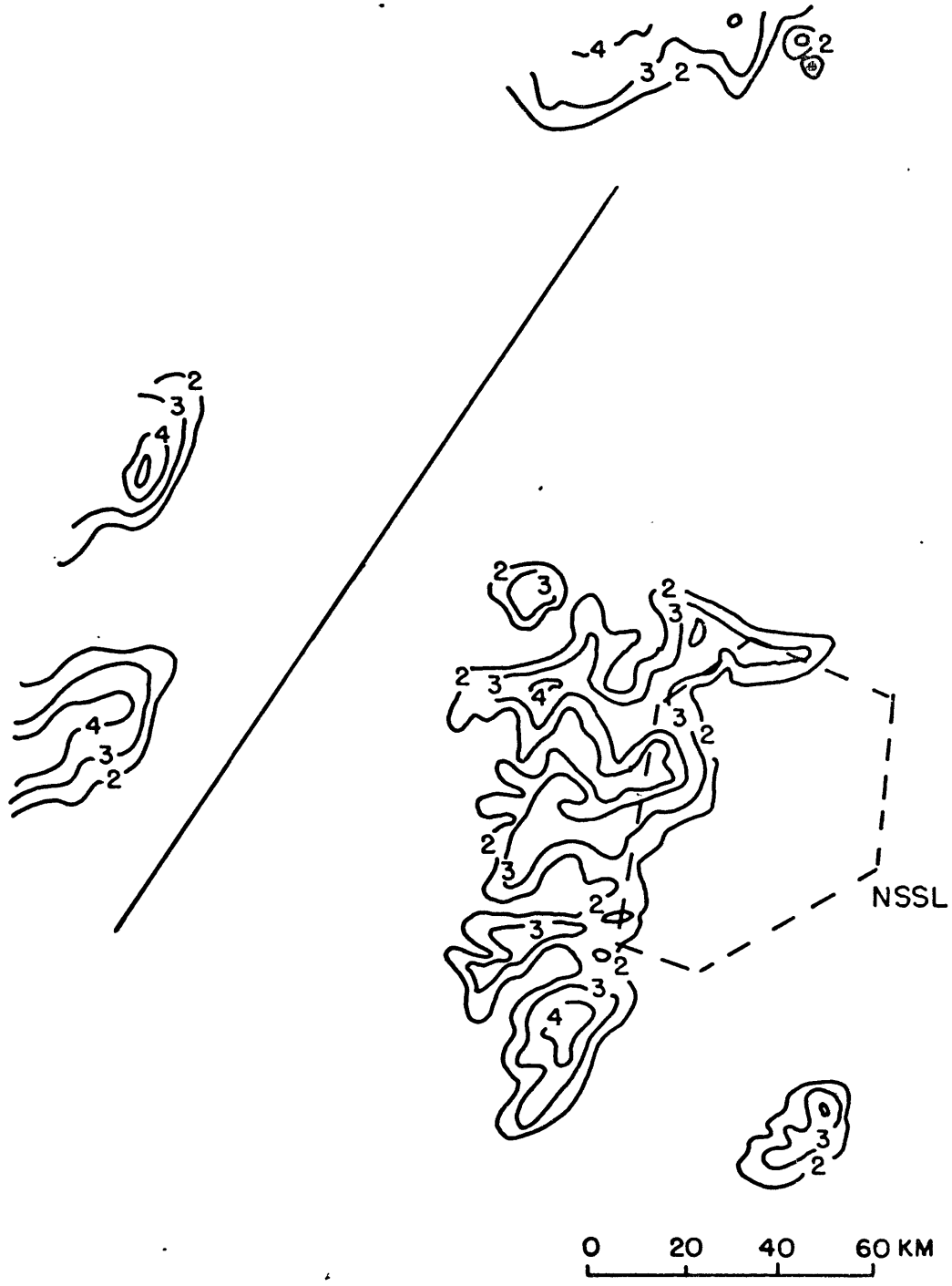

Fig. 6a

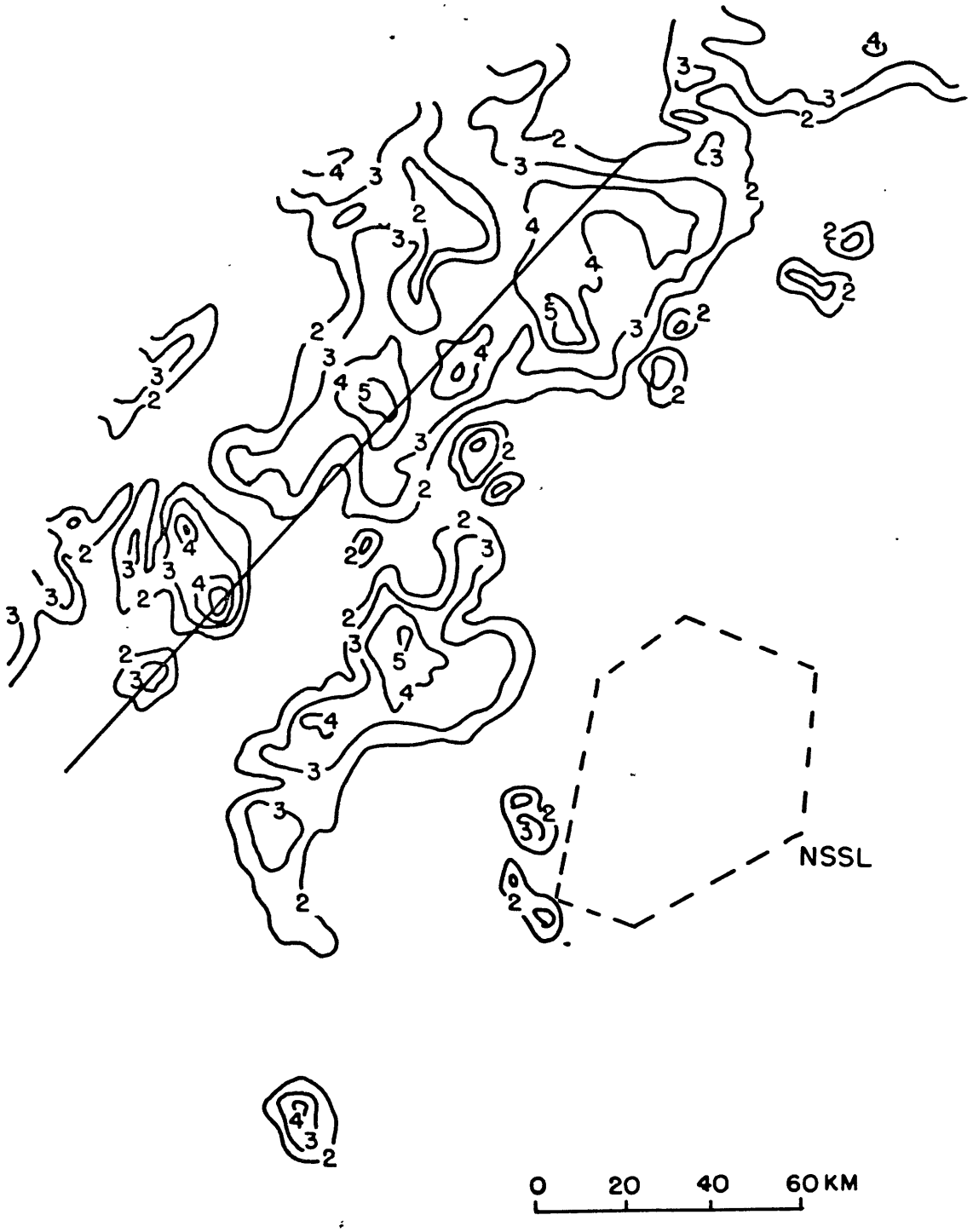

Fig. 6b

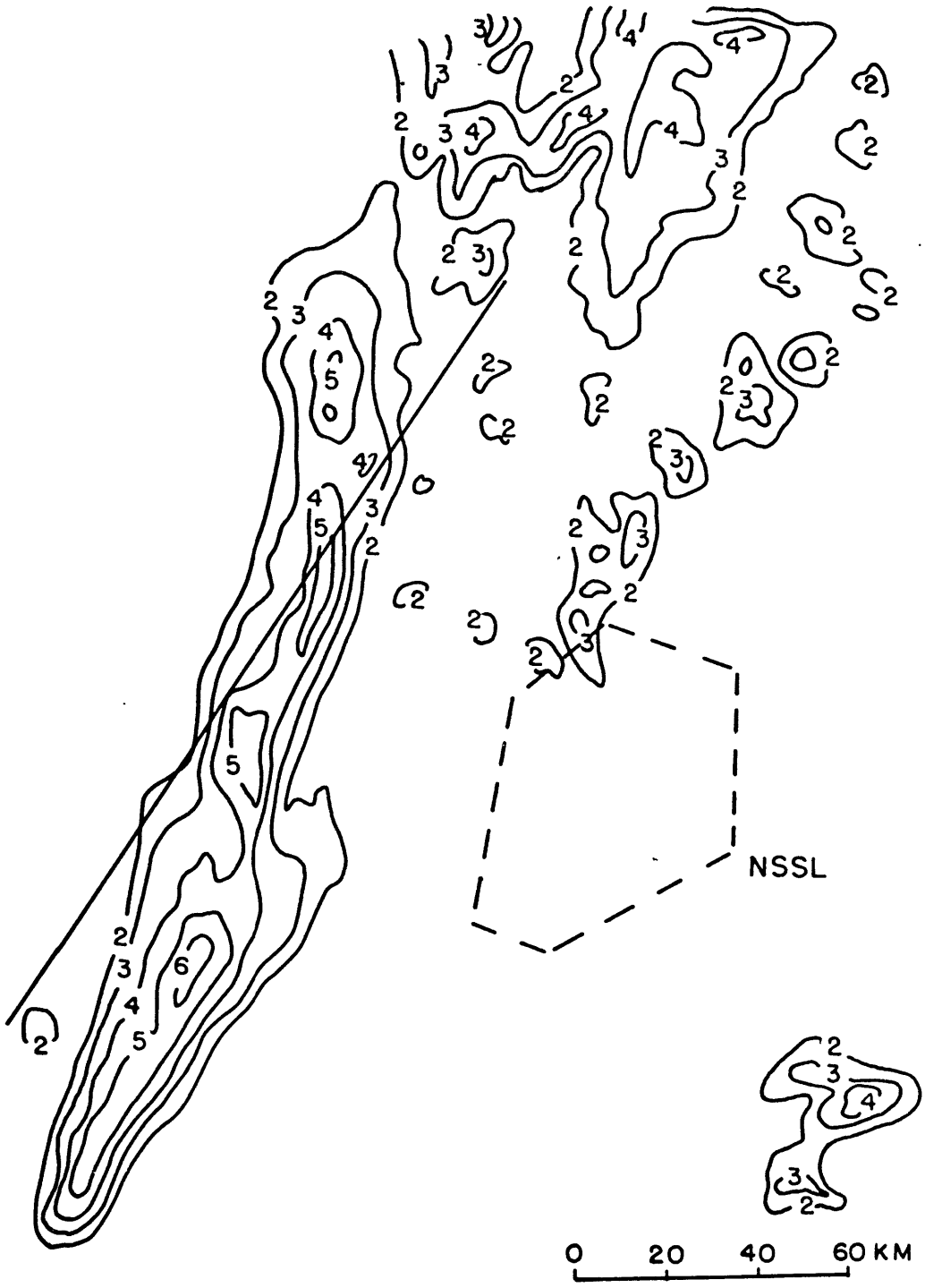

Fig. 6c

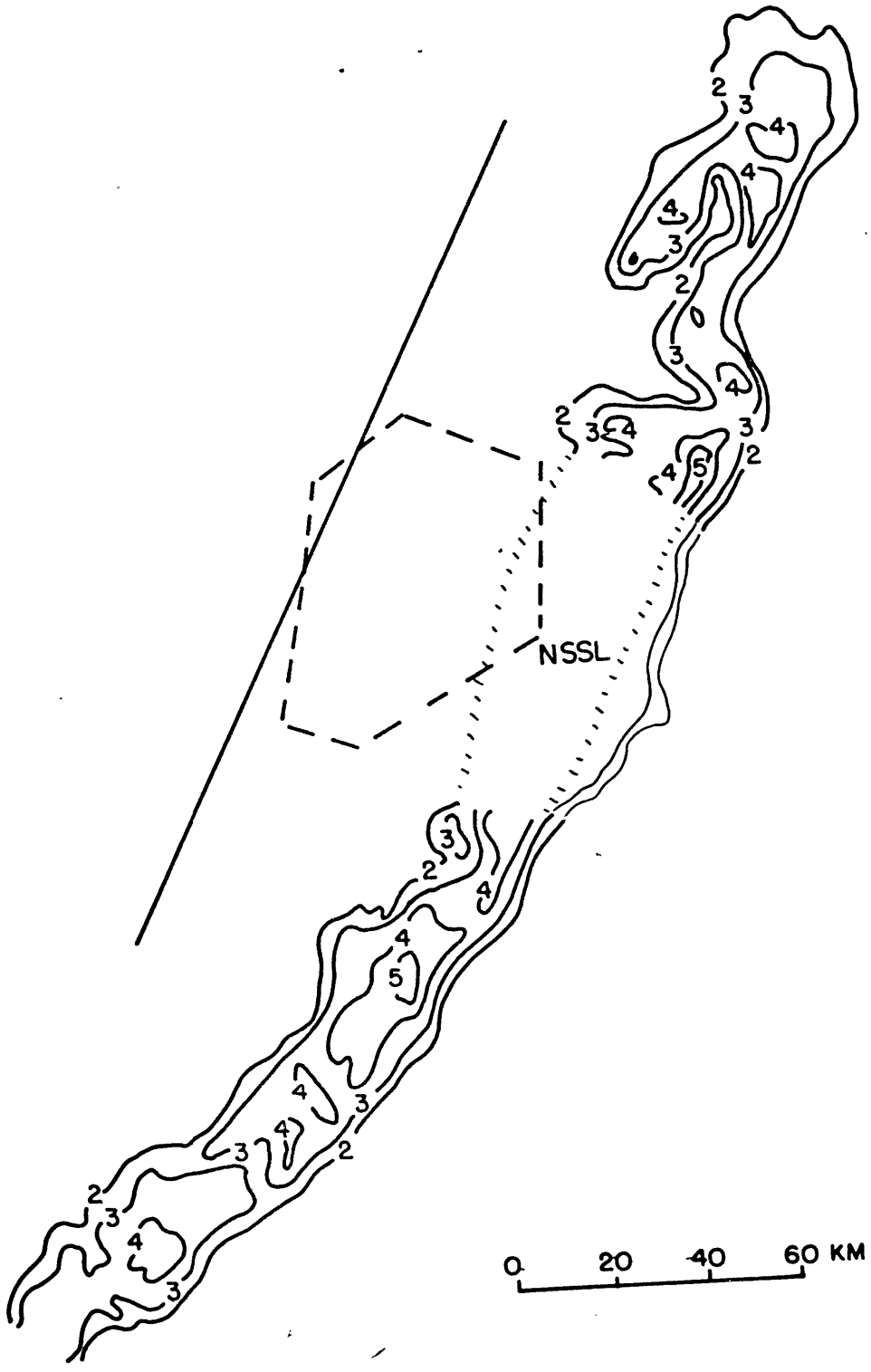

Fig. 6d

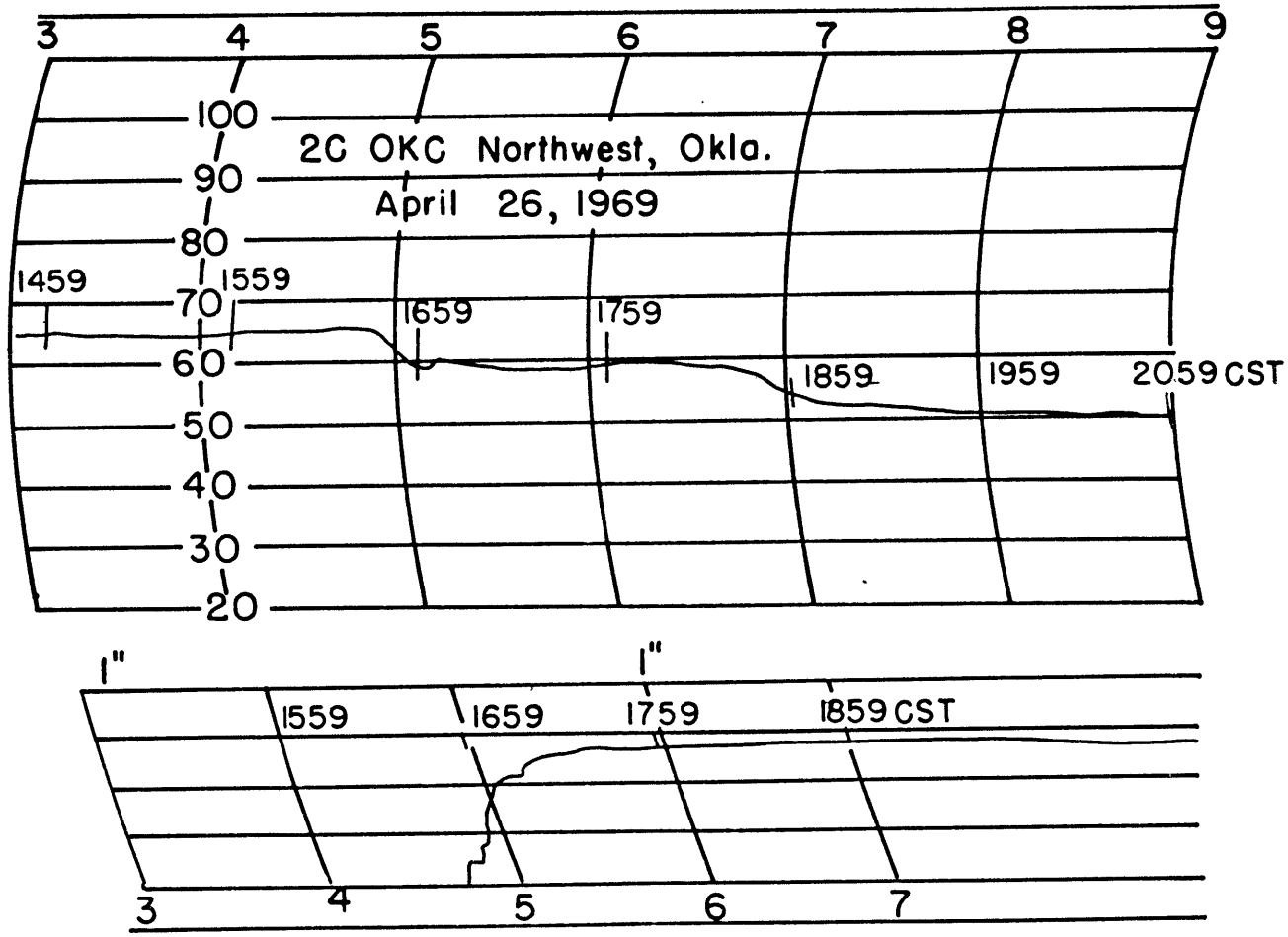
3
4
5
6
7
8
9
100
90
80
70
60
50
40
30
20
2C OKC Northwest, Okla.
April 26, 1969
1459
1559
1659
1759
1859
1959
2059 CST
1"
1"
1559
1659
1759
1859 CST
3
4
5
6
7

Fig. 7

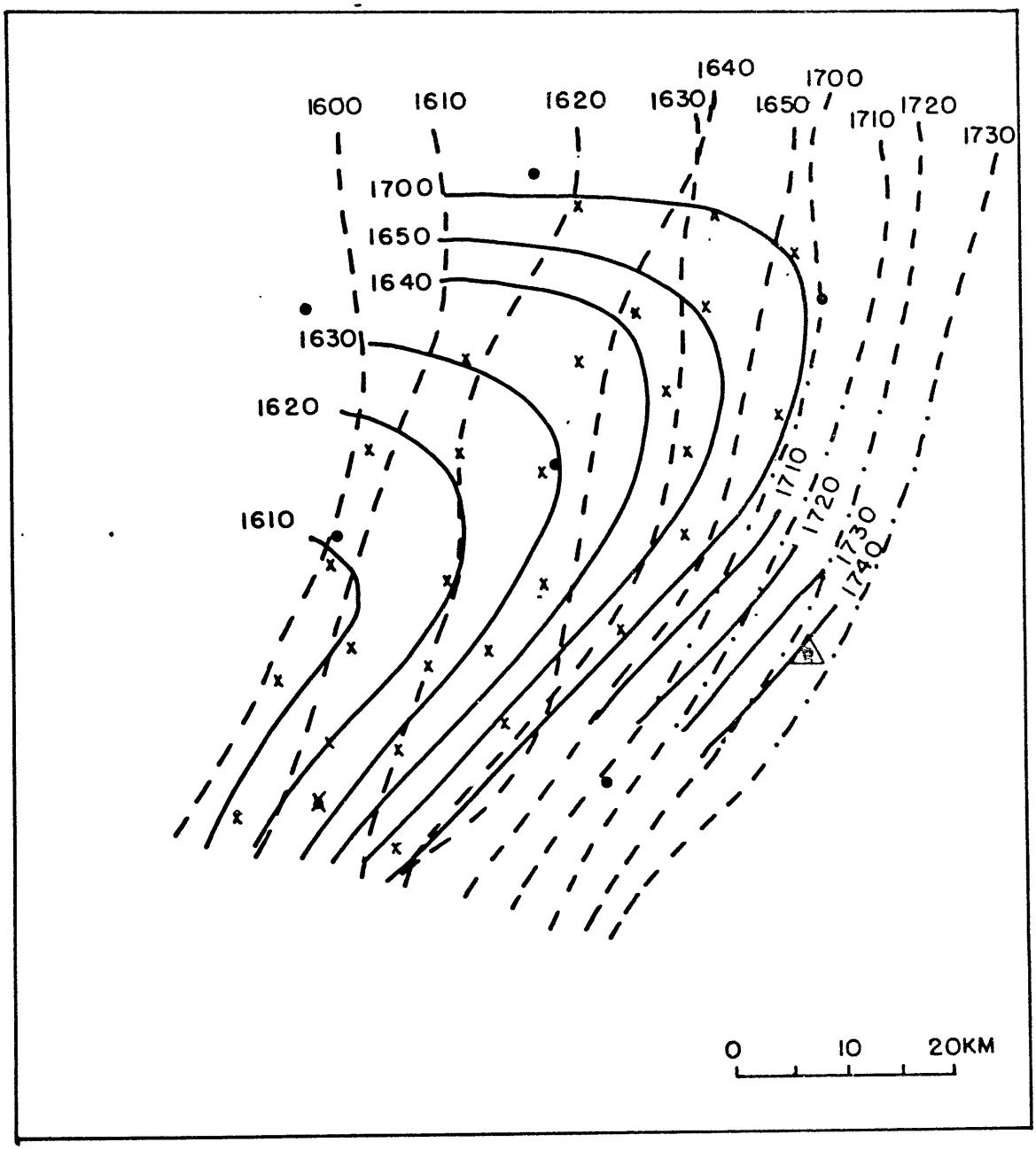
1600
1610
1620
1630
1640
1650
1700
1710
1720
1730
1700
1650
1640
1630
1620
1610
1710
1720
1730
1740
0
10
20KM

Fig. 8

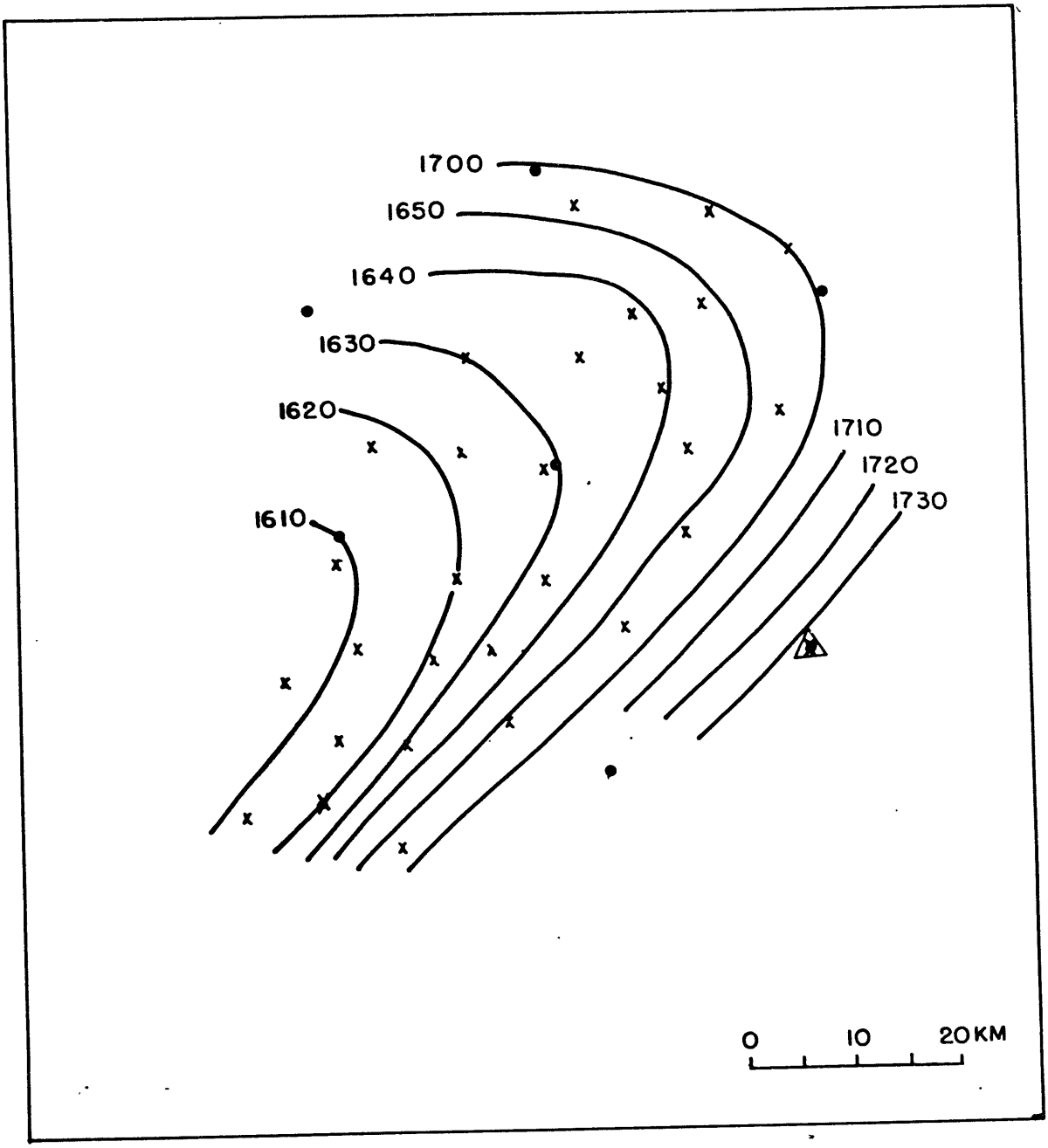

Fig. 9

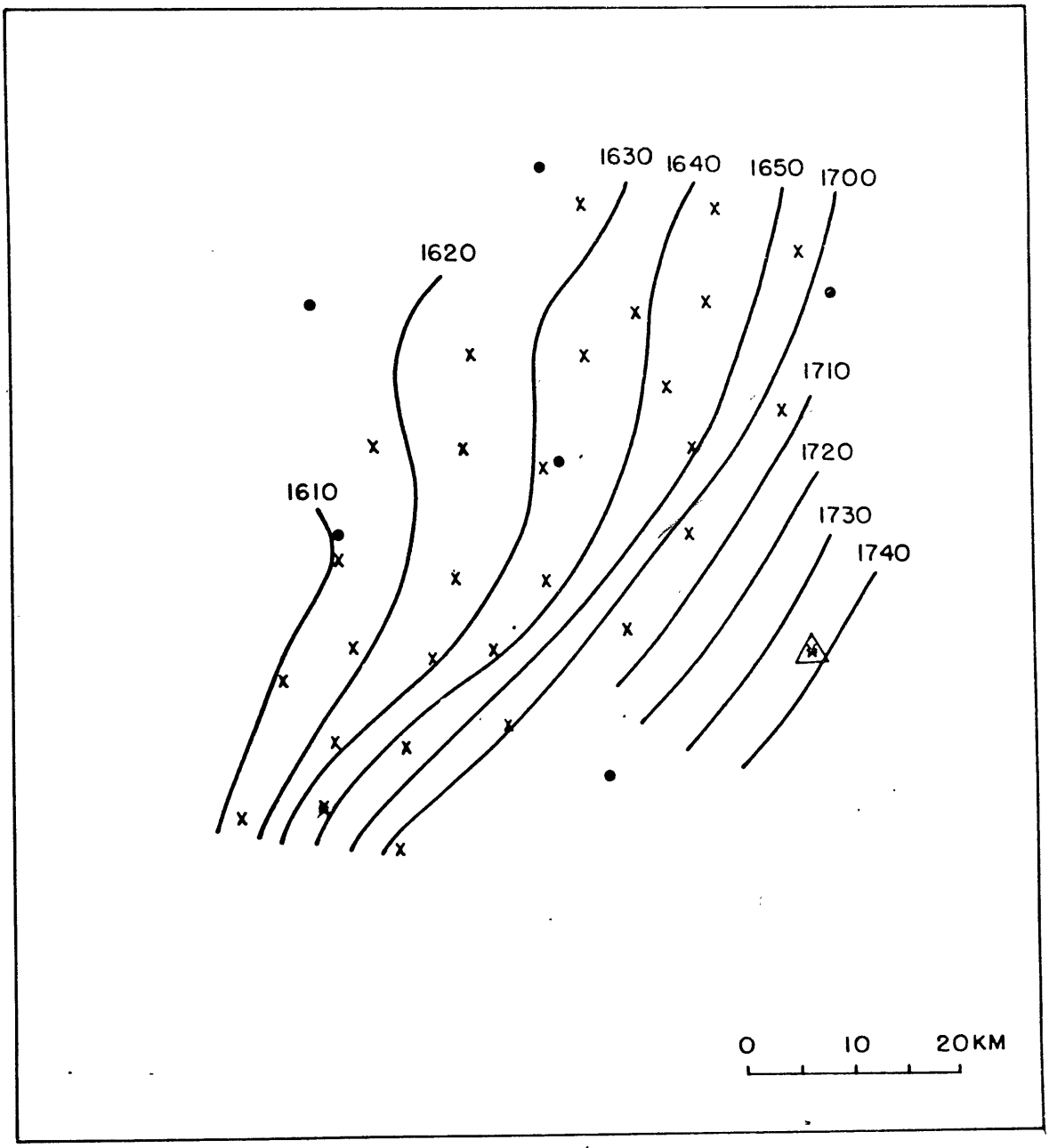

Fig. 10

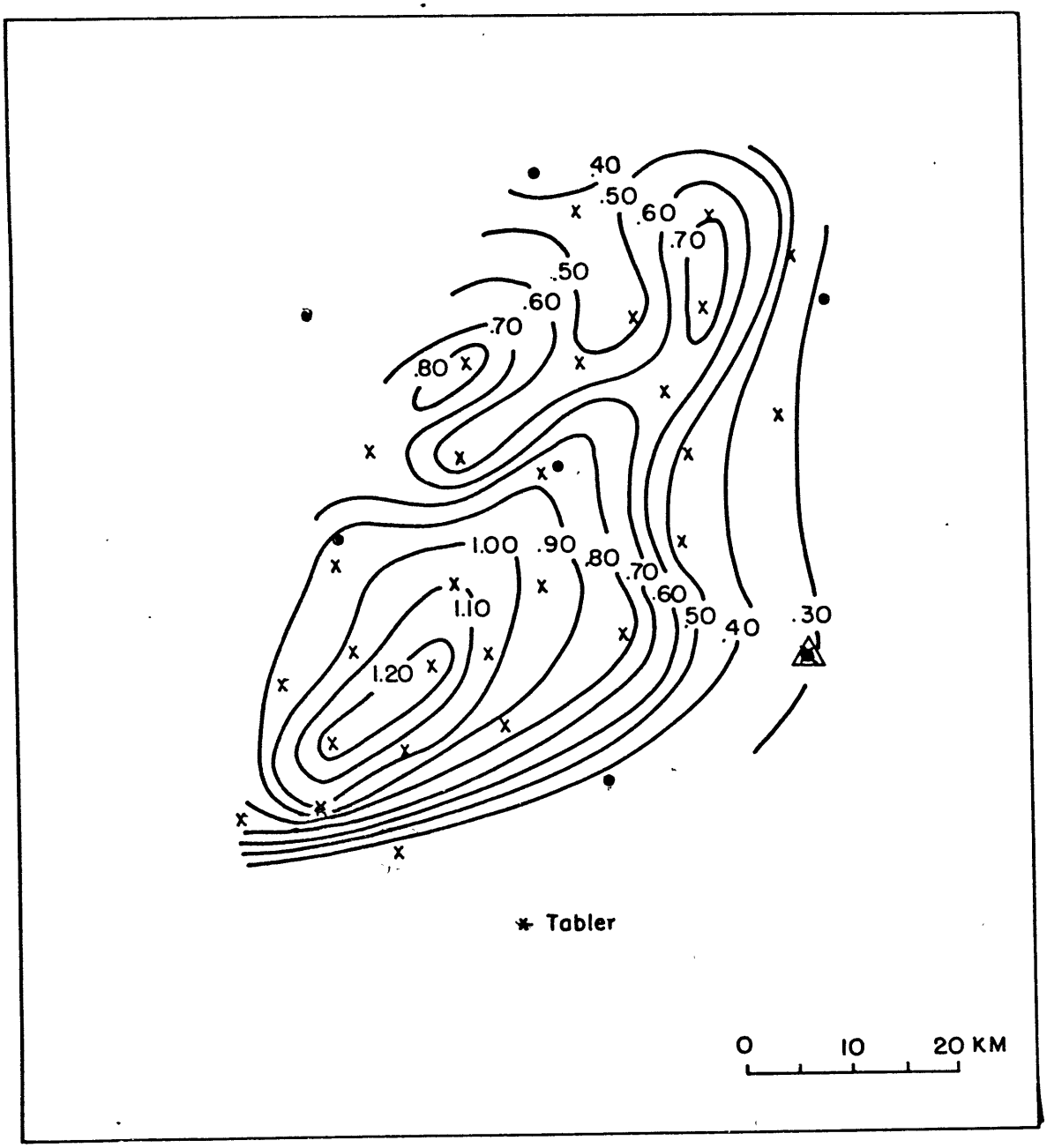
.40
.50
.60
.70
.50
.60
.70
.80
1.00
.90
.80
.70
.60
.50
.40
.30
1.10
1.20
* Tabler
0
10
20 KM

Fig. 11

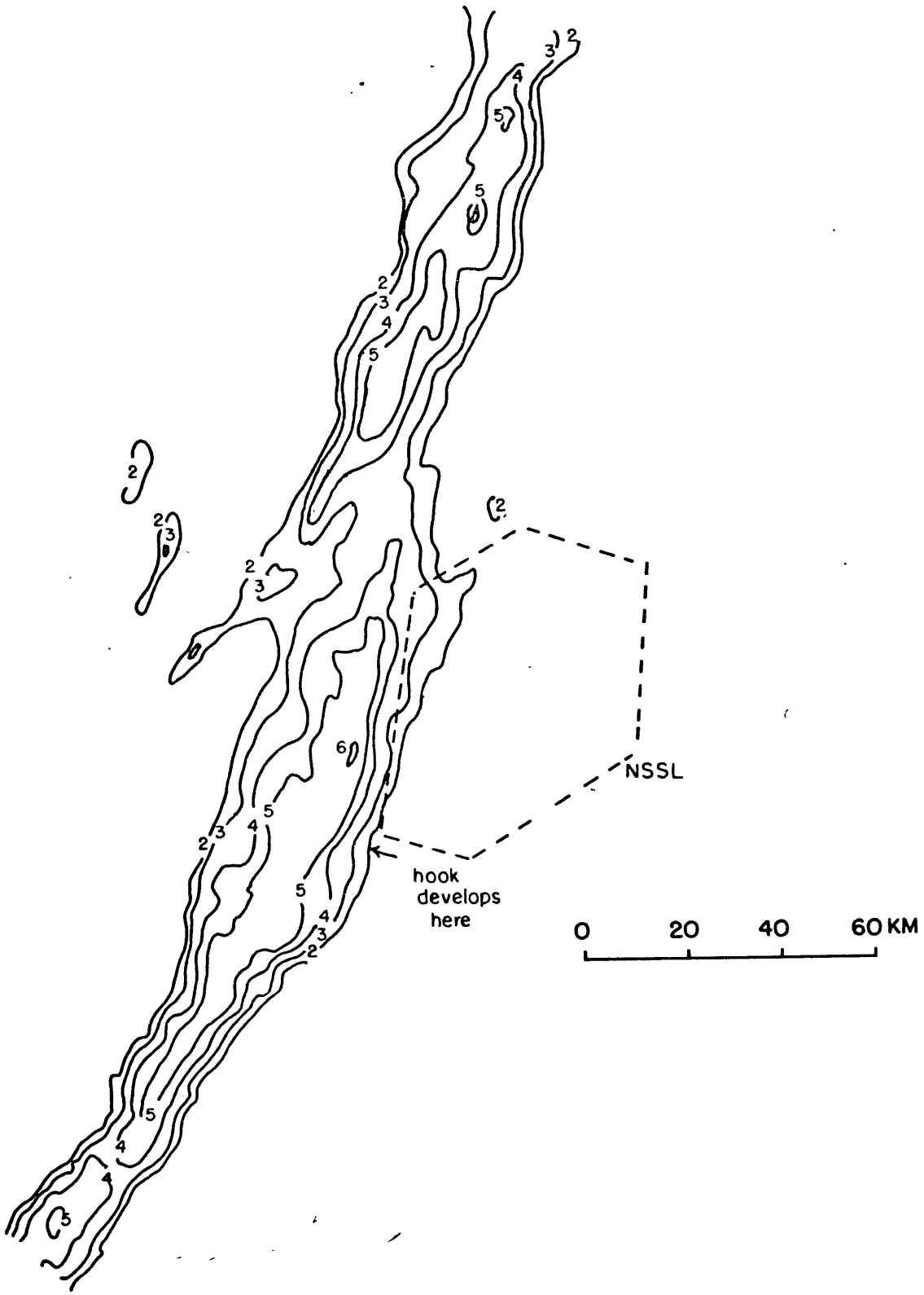

Fig. 12a

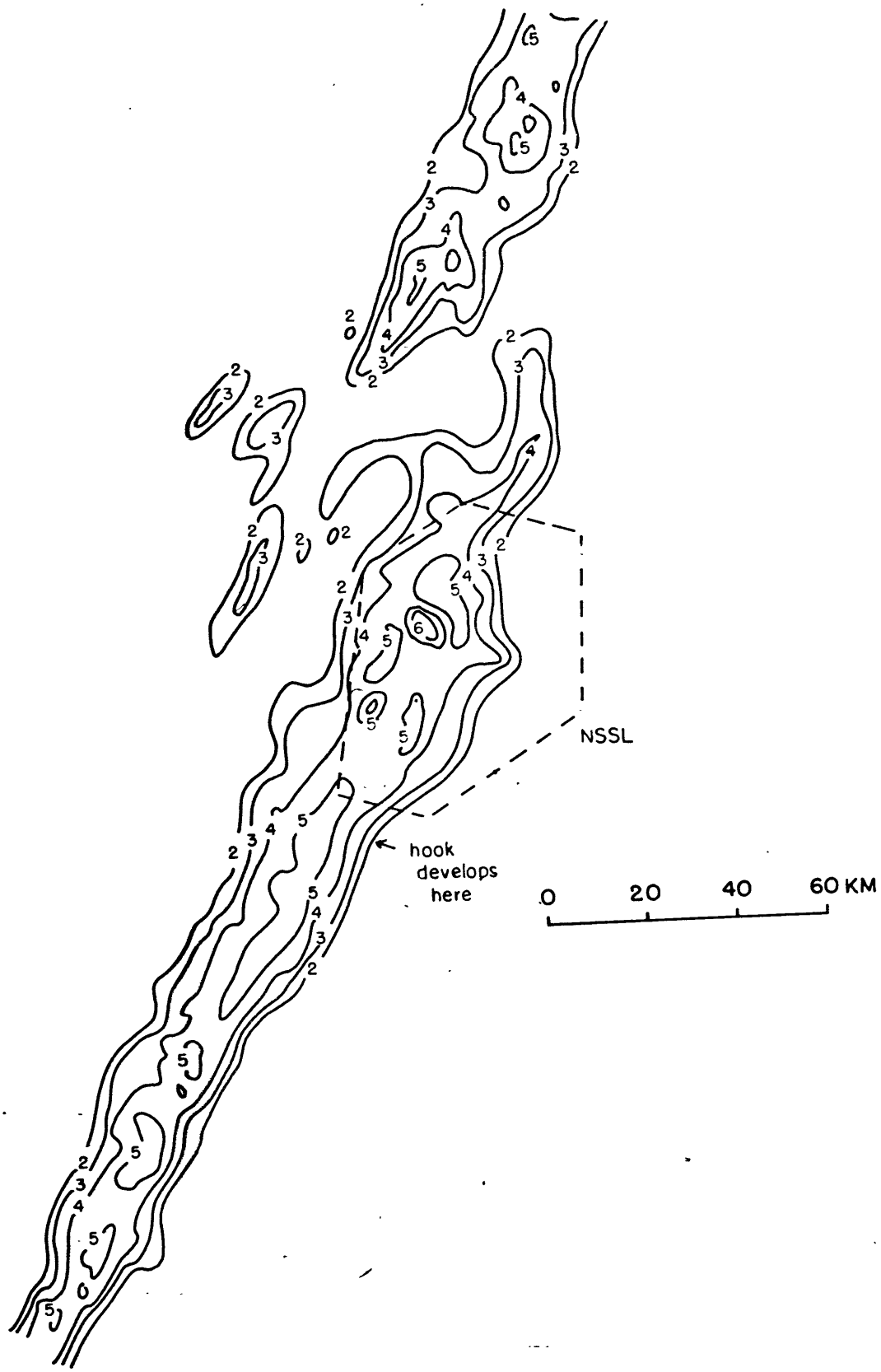

Fig. 12b

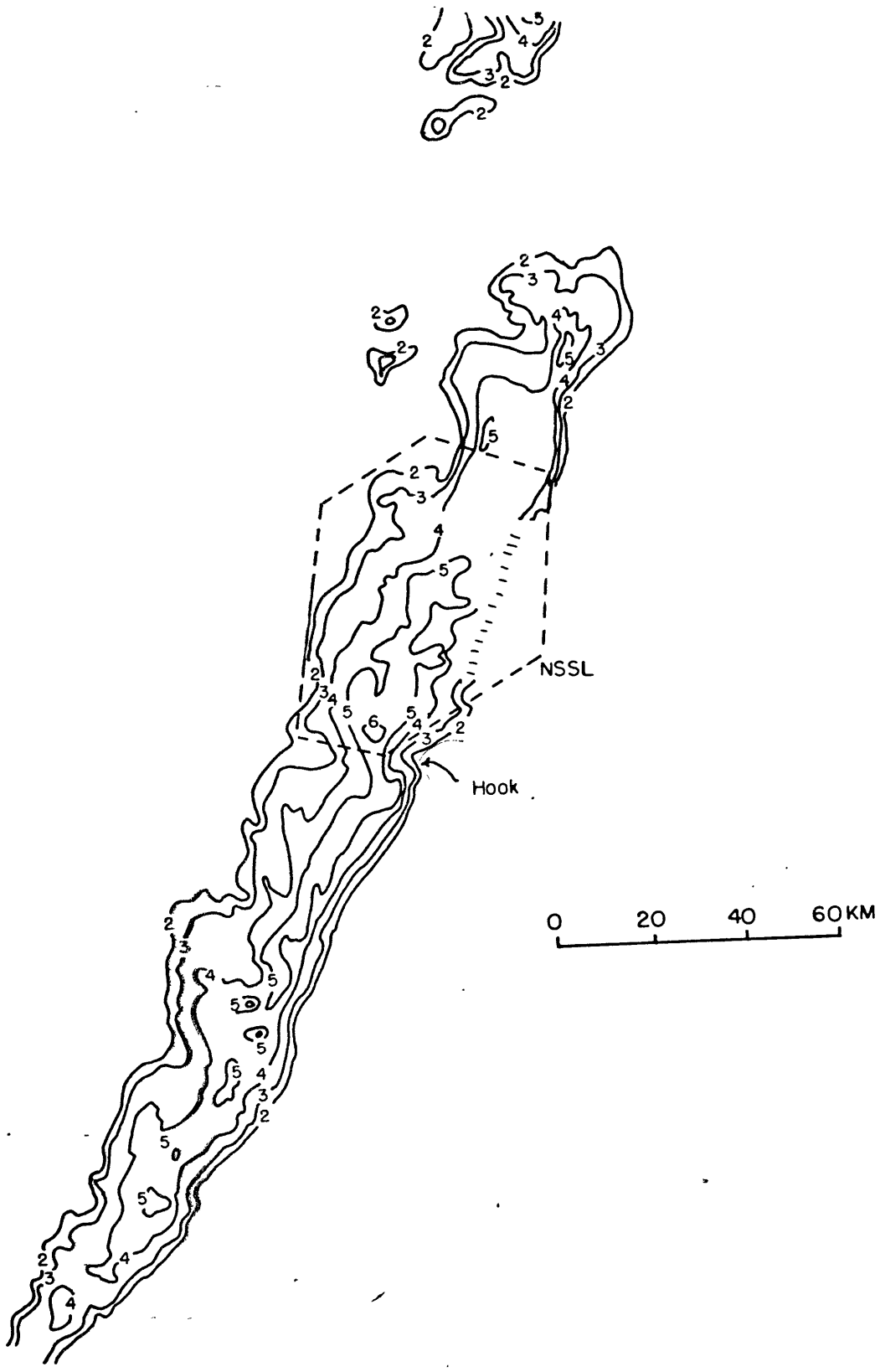

Fig. 12c

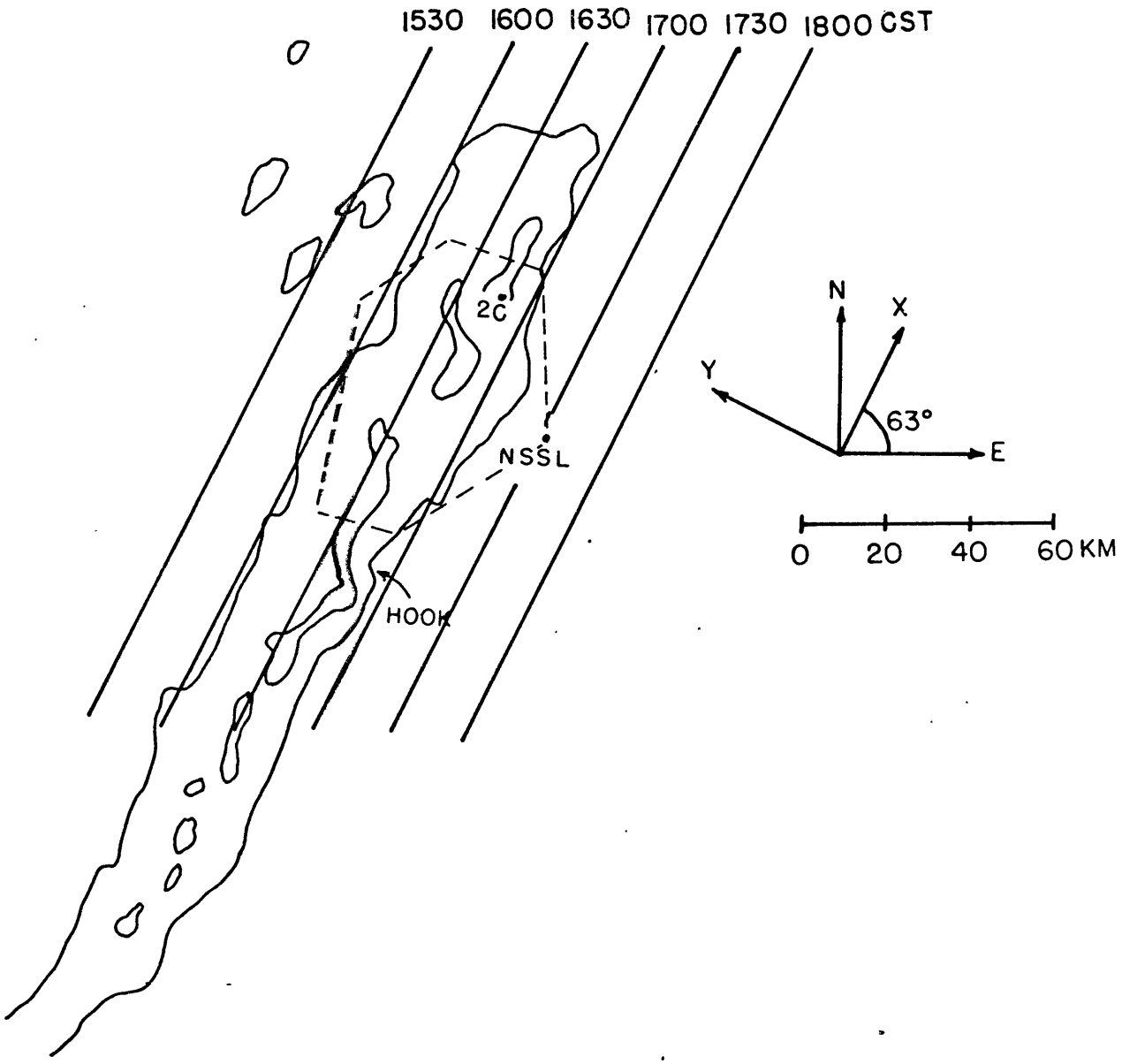
1530
1600
1630
1700
1730
1800 CST
2C
NSSL
HOOK
N
X
Y
63°
E
0
20
40
60 KM

Fig. 13

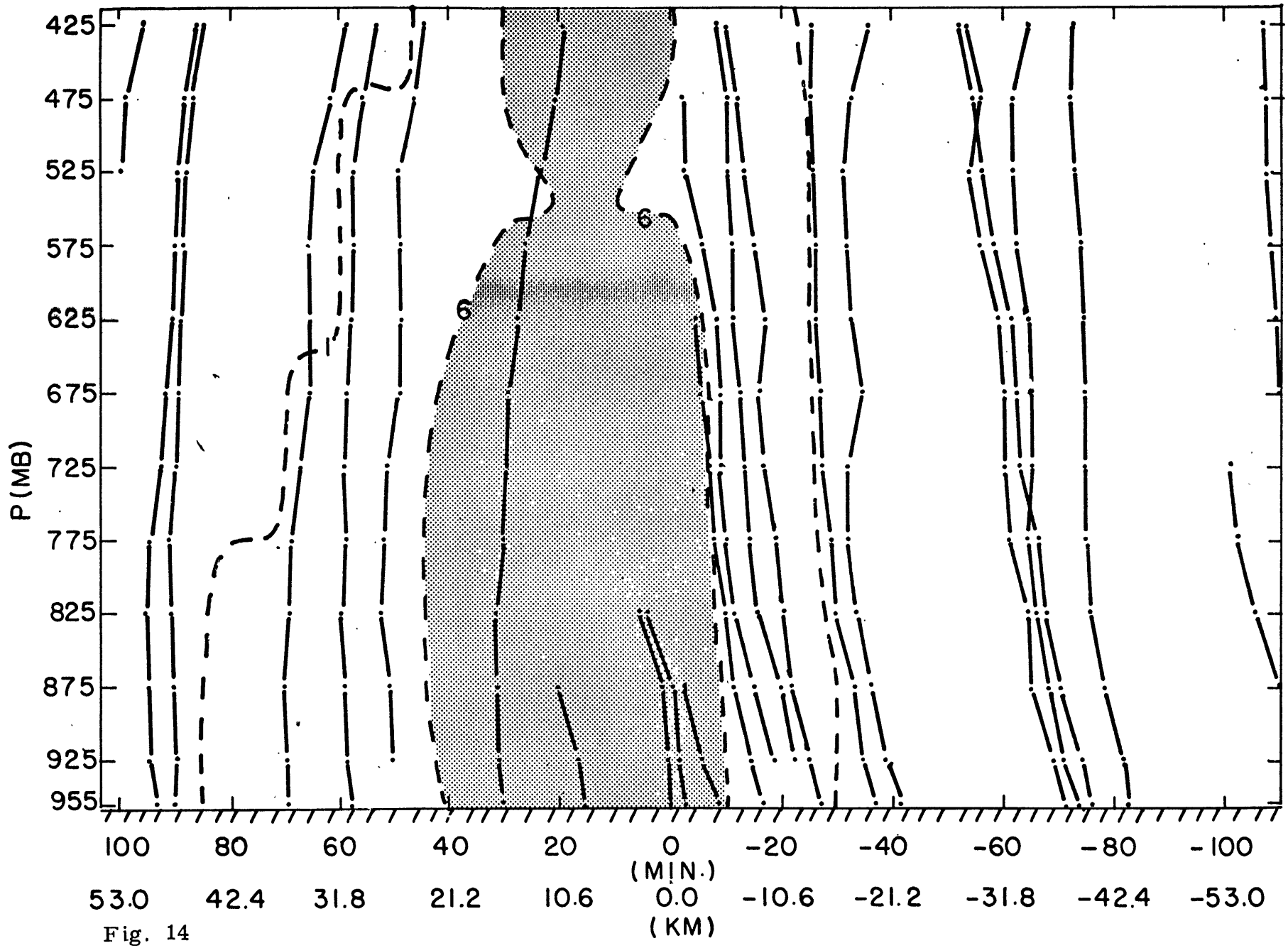
425
475
525
575
625
675
725
775
825
875
925
955
P(MB)
6
6
100
80
60
40
20
0
-20
-40
-60
-80
-100
(MIN.)
53.0
42.4
31.8
21.2
10.6
0.0
-10.6
-21.2
-31.8
-42.4
-53.0
(KM)

Fig. 14

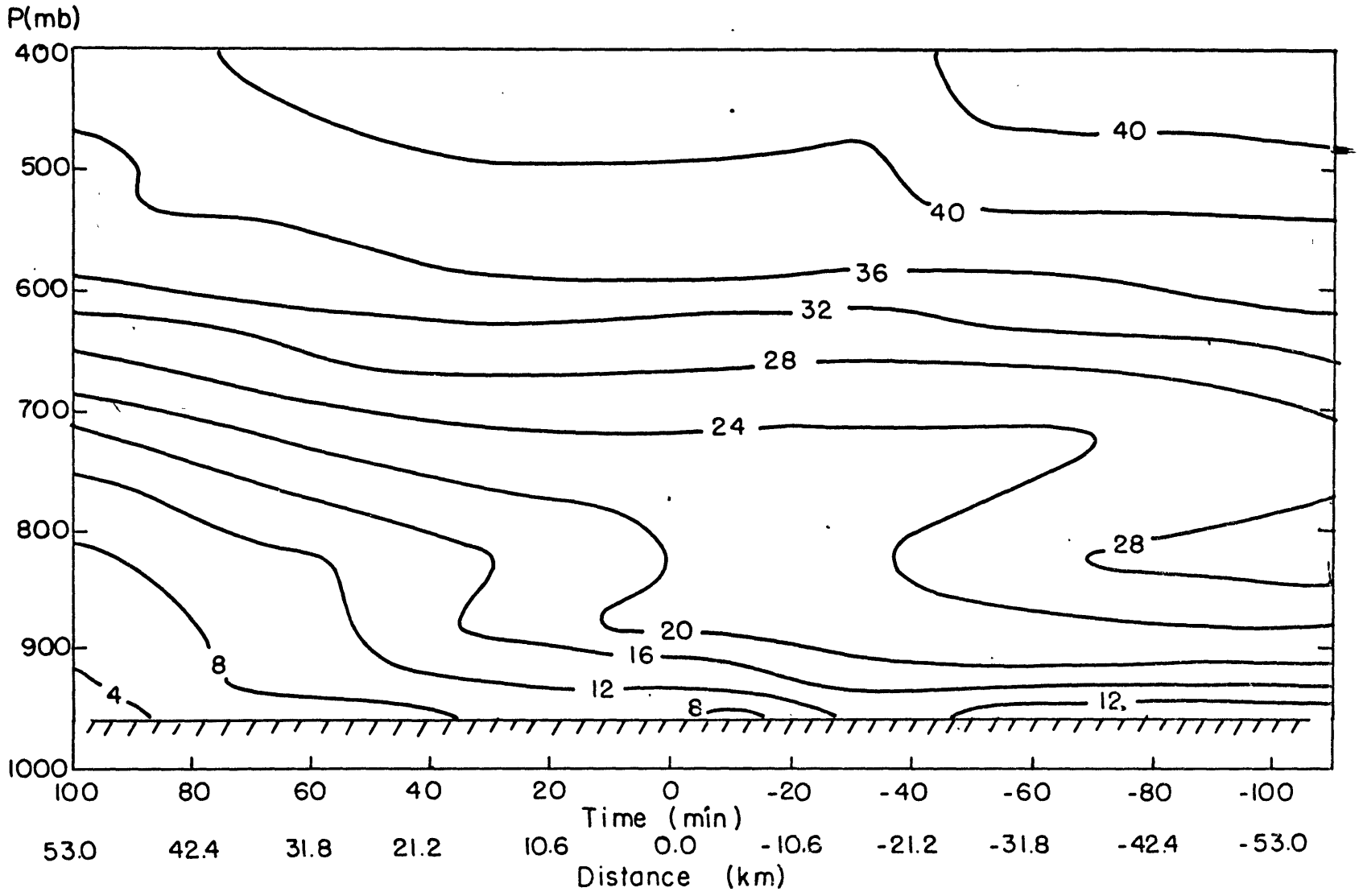
P(mb)
400
500
600
700
800
900
1000
40
40
36
32
28
24
28
20
16
12
8
4
8
12
100
80
60
40
20
0
-20
-40
-60
-80
-100
Time (min)
53.0
42.4
31.8
21.2
10.6
0.0
-10.6
-21.2
-31.8
-42.4
-53.0
Distance (km)

Fig. 15

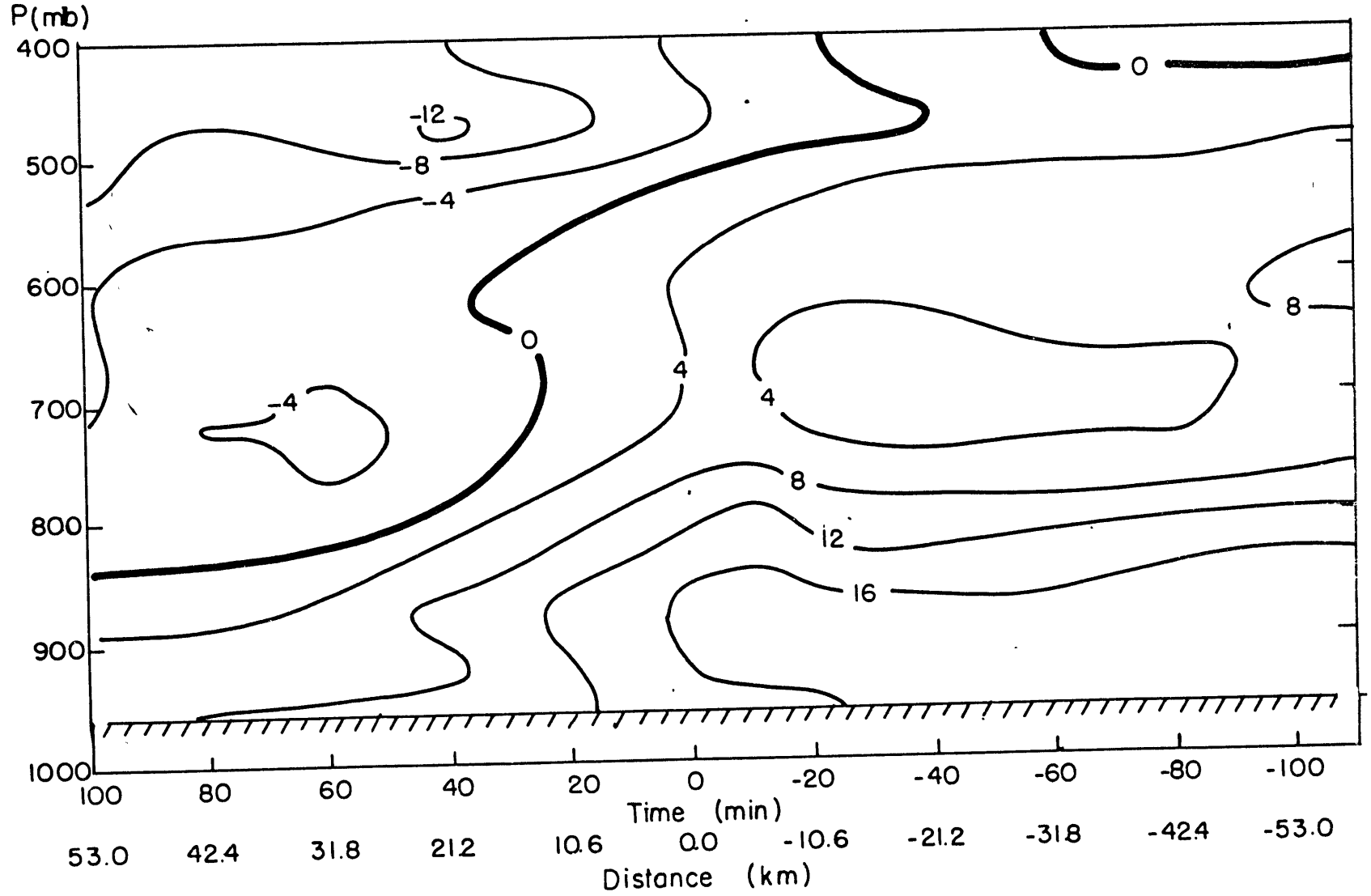
P(mb)
400
500
600
700
800
900
1000
-12
-8
-4
0
4
8
12
16
100
80
60
40
20
0
-20
-40
-60
-80
-100
Time (min)
53.0
42.4
31.8
21.2
10.6
0.0
-10.6
-21.2
-31.8
-42.4
-53.0
Distance (km)

Fig. 16

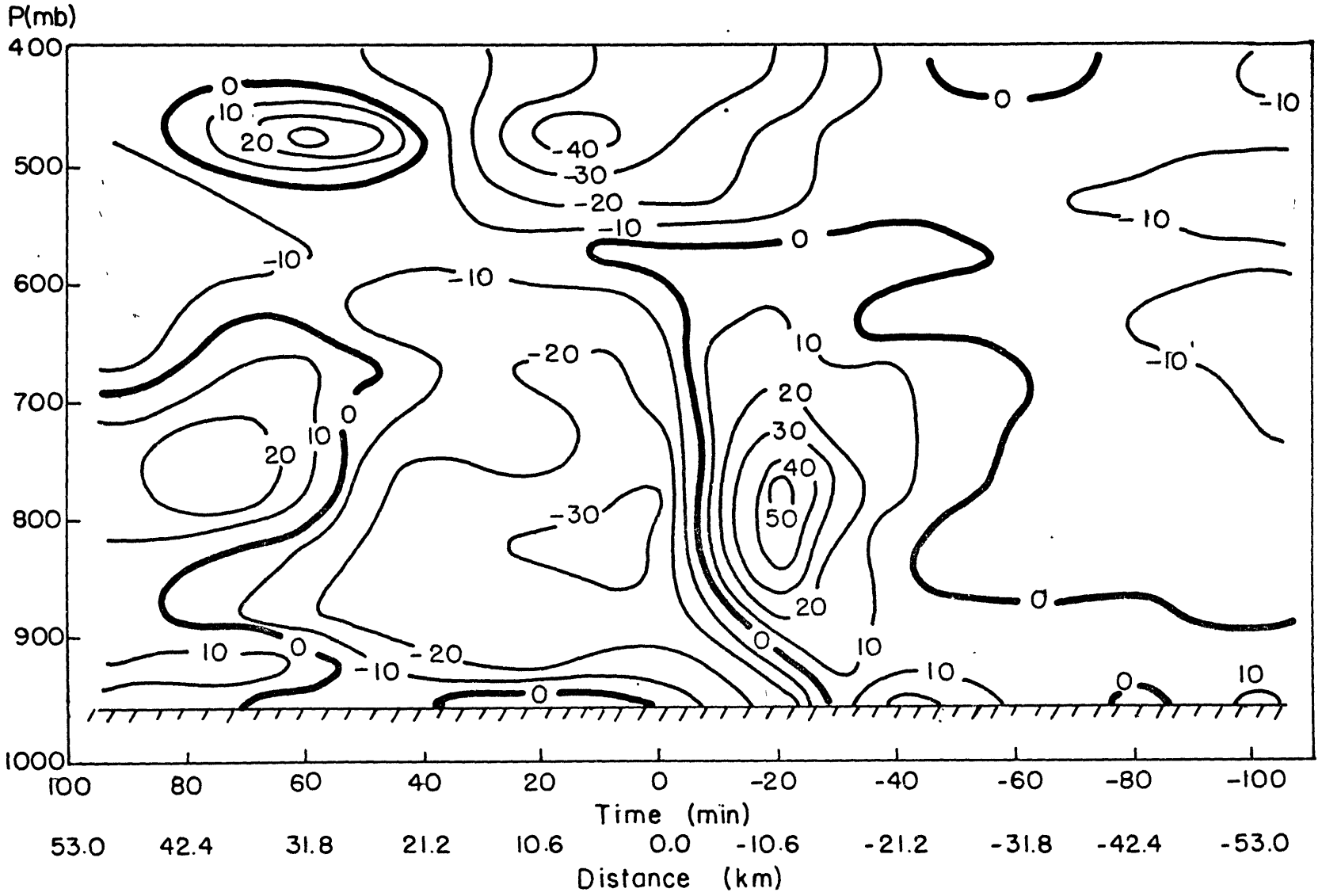
P(mb)
400
500
600
700
800
900
1000
100
80
60
40
20
0
-20
-40
-60
-80
-100
Time (min)
53.0
42.4
31.8
21.2
10.6
0.0
-10.6
-21.2
-31.8
-42.4
-53.0
Distance (km)

Fig. 17

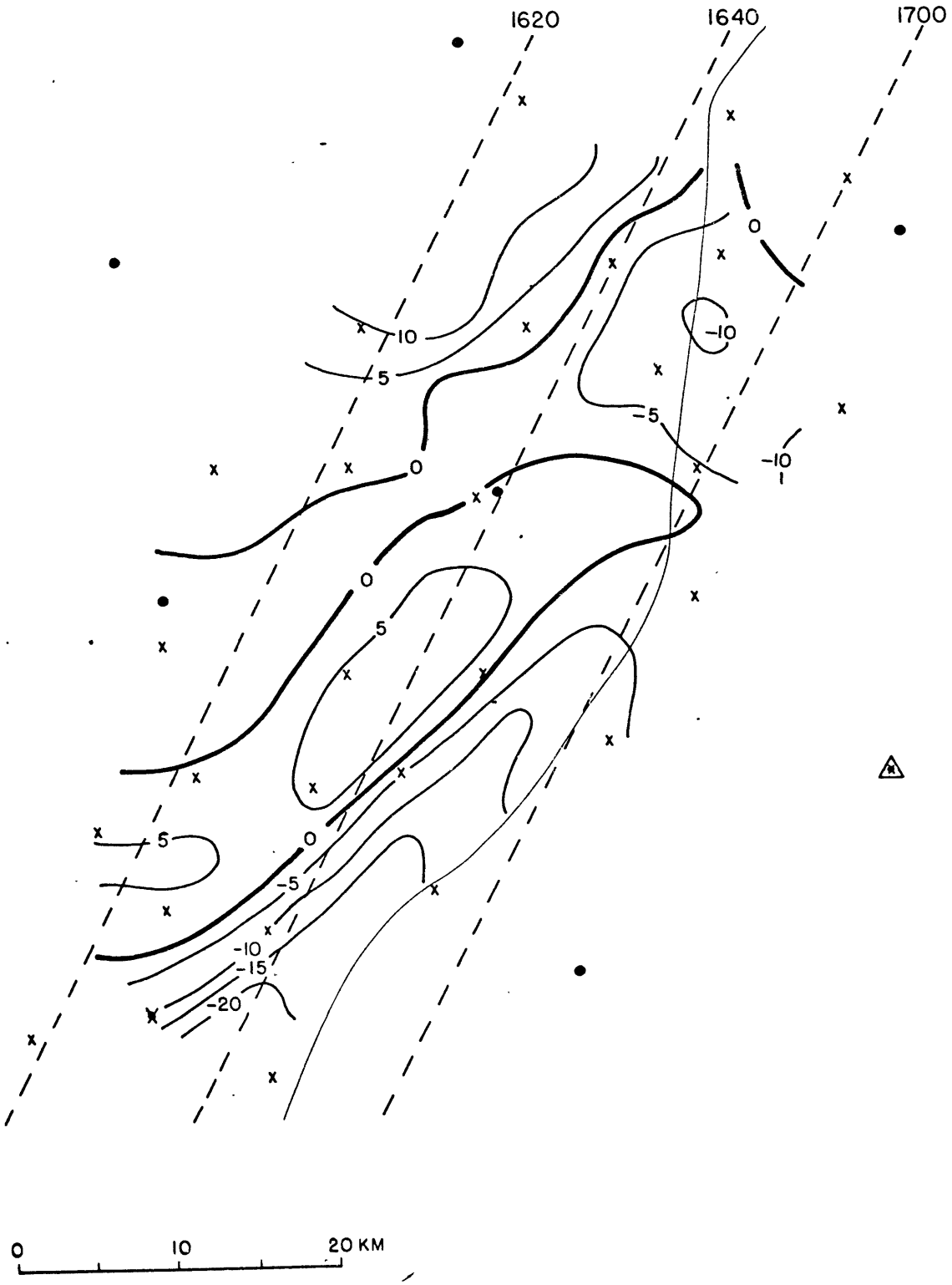

Fig. 18

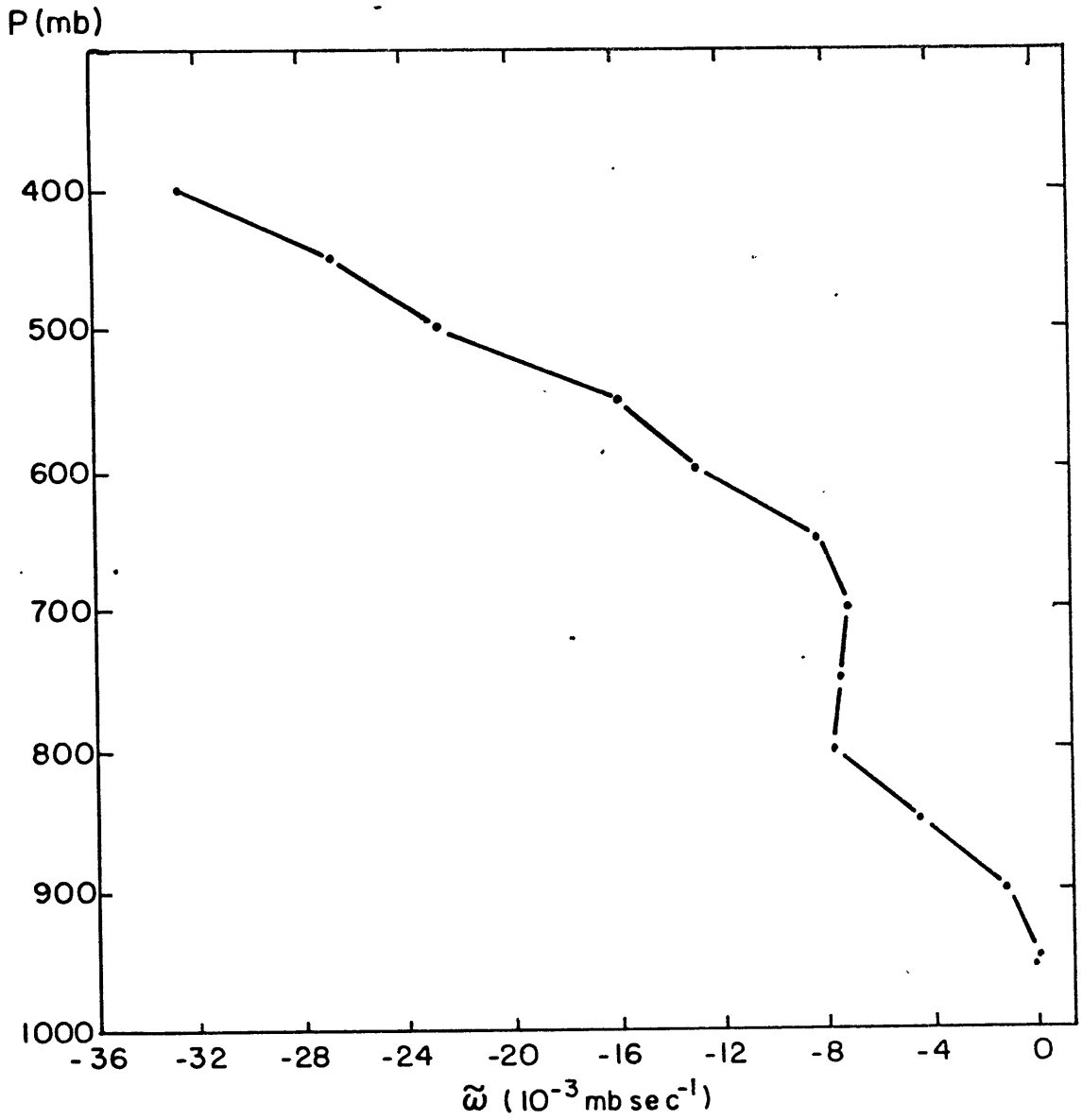
P (mb)
400
500
600
700
800
900
1000
-36
-32
-28
-24
-20
-16
-12
-8
-4
0
$\tilde{\omega}$ (10^{-3} mb sec^{-1})

Fig. 19

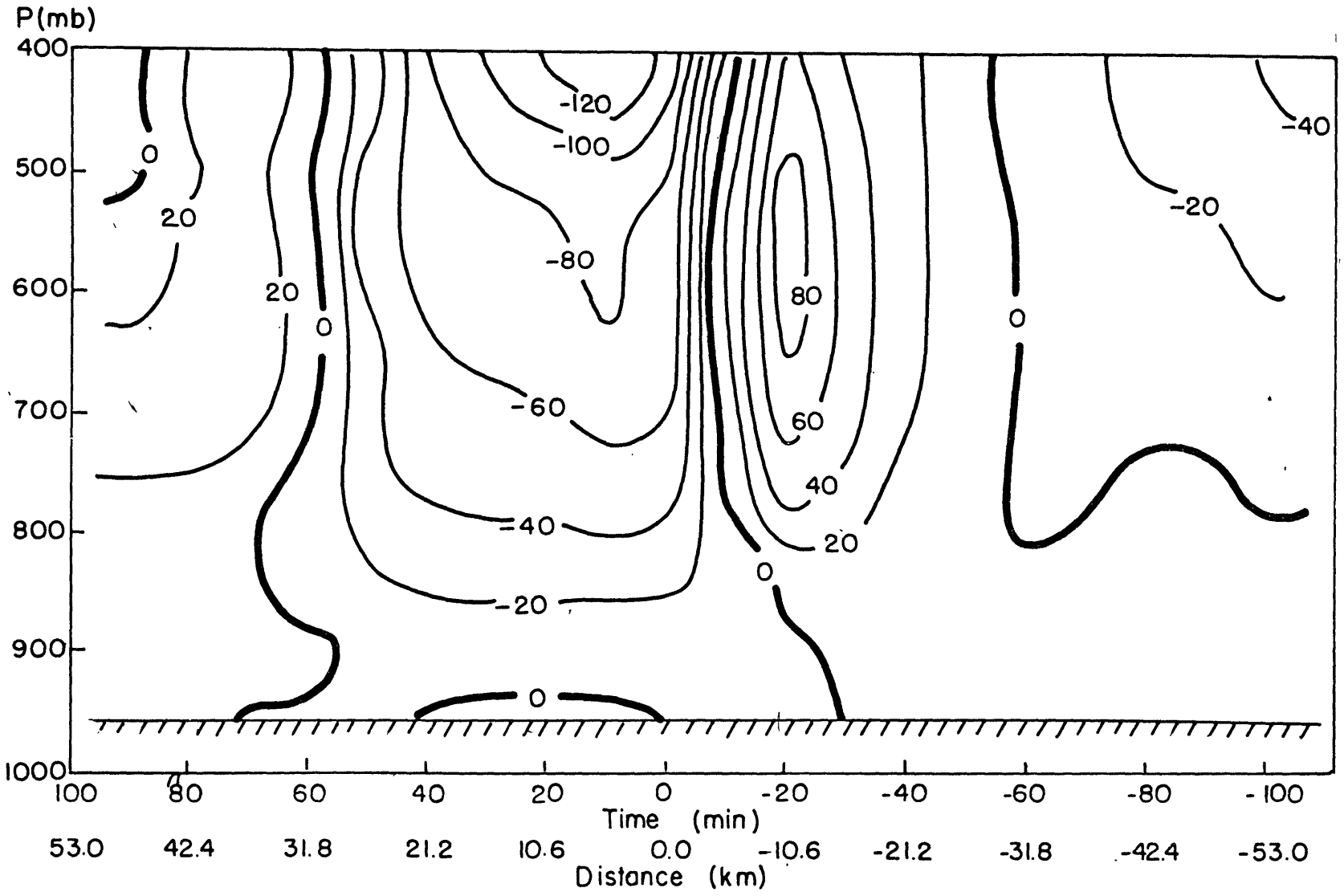
P(mb)
400
500
600
700
800
900
1000
0
20
20
0
-120
-100
-80
-60
-40
-20
0
80
60
40
20
0
0
-40
-20
100
80
60
40
20
0
-20
-40
-60
-80
-100
Time (min)
53.0
42.4
31.8
21.2
10.6
0.0
-10.6
-21.2
-31.8
-42.4
-53.0
Distance (km)

Fig. 20

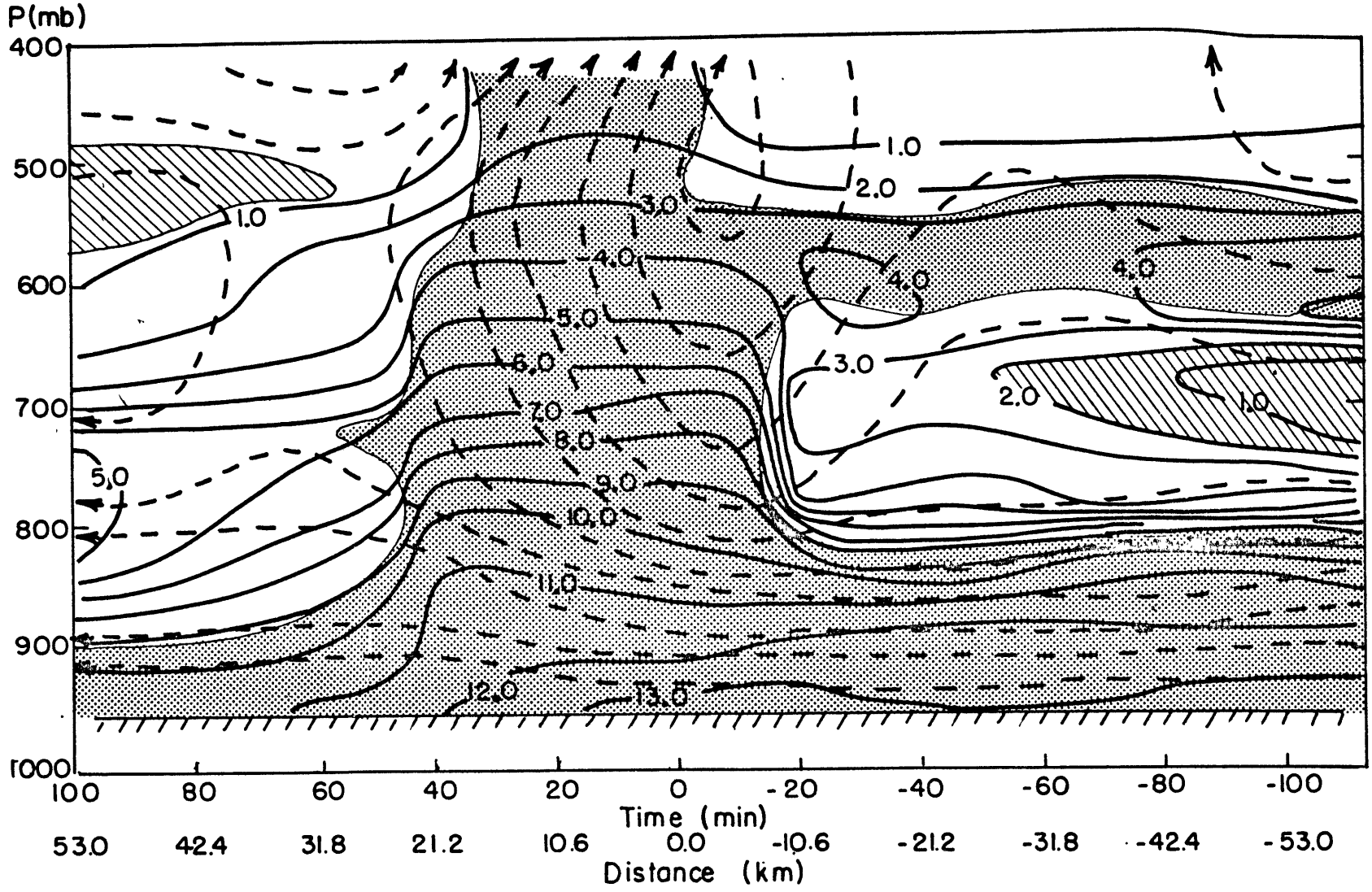
P(mb)
400
500
600
700
800
900
1000
1.0
2.0
3.0
4.0
5.0
6.0
7.0
8.0
9.0
10.0
11.0
12.0
13.0
100
80
60
40
20
0
-20
-40
-60
-80
-100
Time (min)
53.0
42.4
31.8
21.2
10.6
0.0
-10.6
-21.2
-31.8
-42.4
-53.0
Distance (km)

Fig. 21

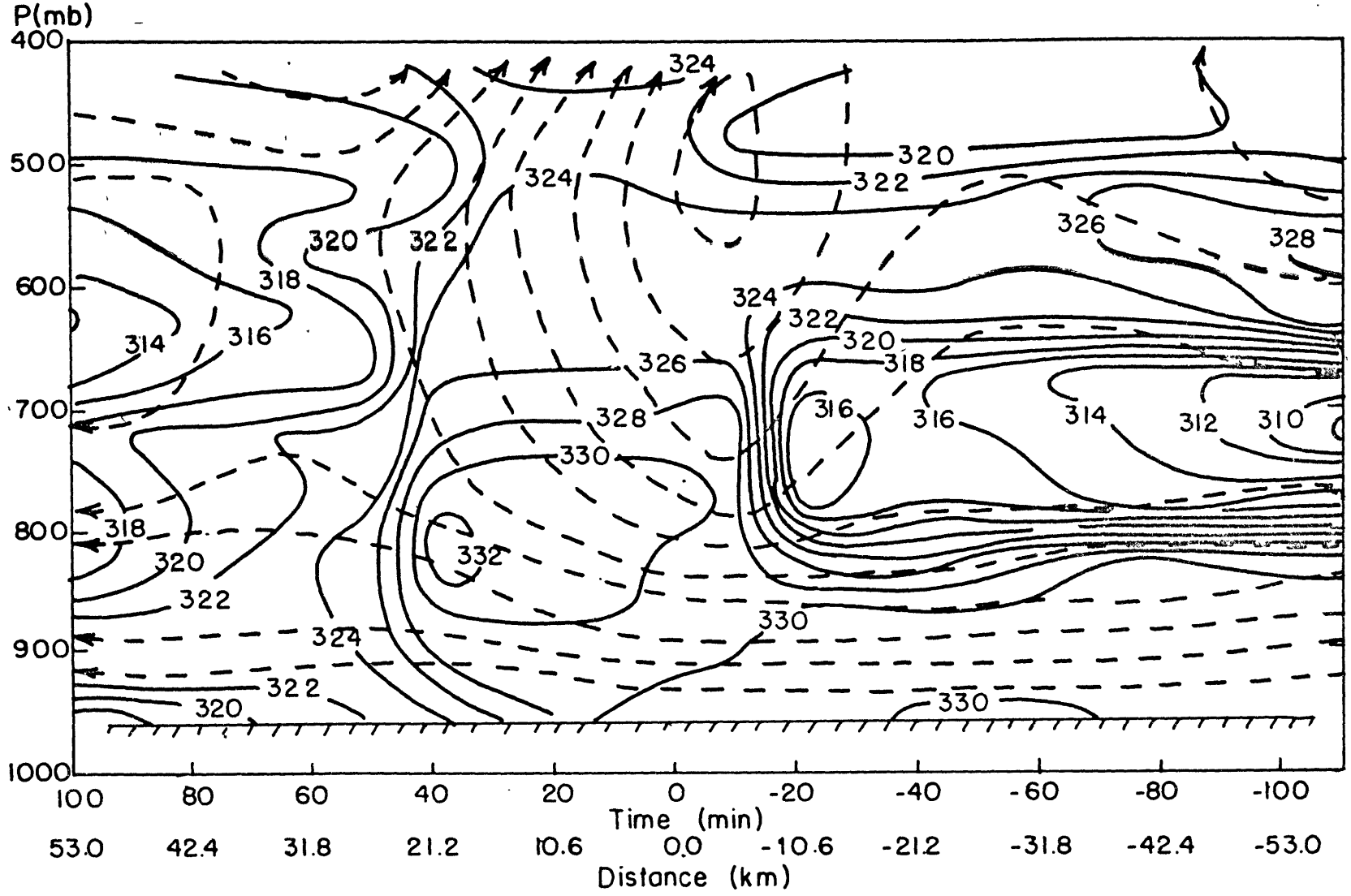
P(mb)
400
500
600
700
800
900
1000
324
320
322
324
326
328
320
322
318
314
316
324
322
320
318
326
328
316
316
314
312
310
330
318
320
322
332
330
324
322
320
330
100
80
60
40
20
0
-20
-40
-60
-80
-100
Time (min)
53.0
42.4
31.8
21.2
10.6
0.0
-10.6
-21.2
-31.8
-42.4
-53.0
Distance (km)

Fig. 22

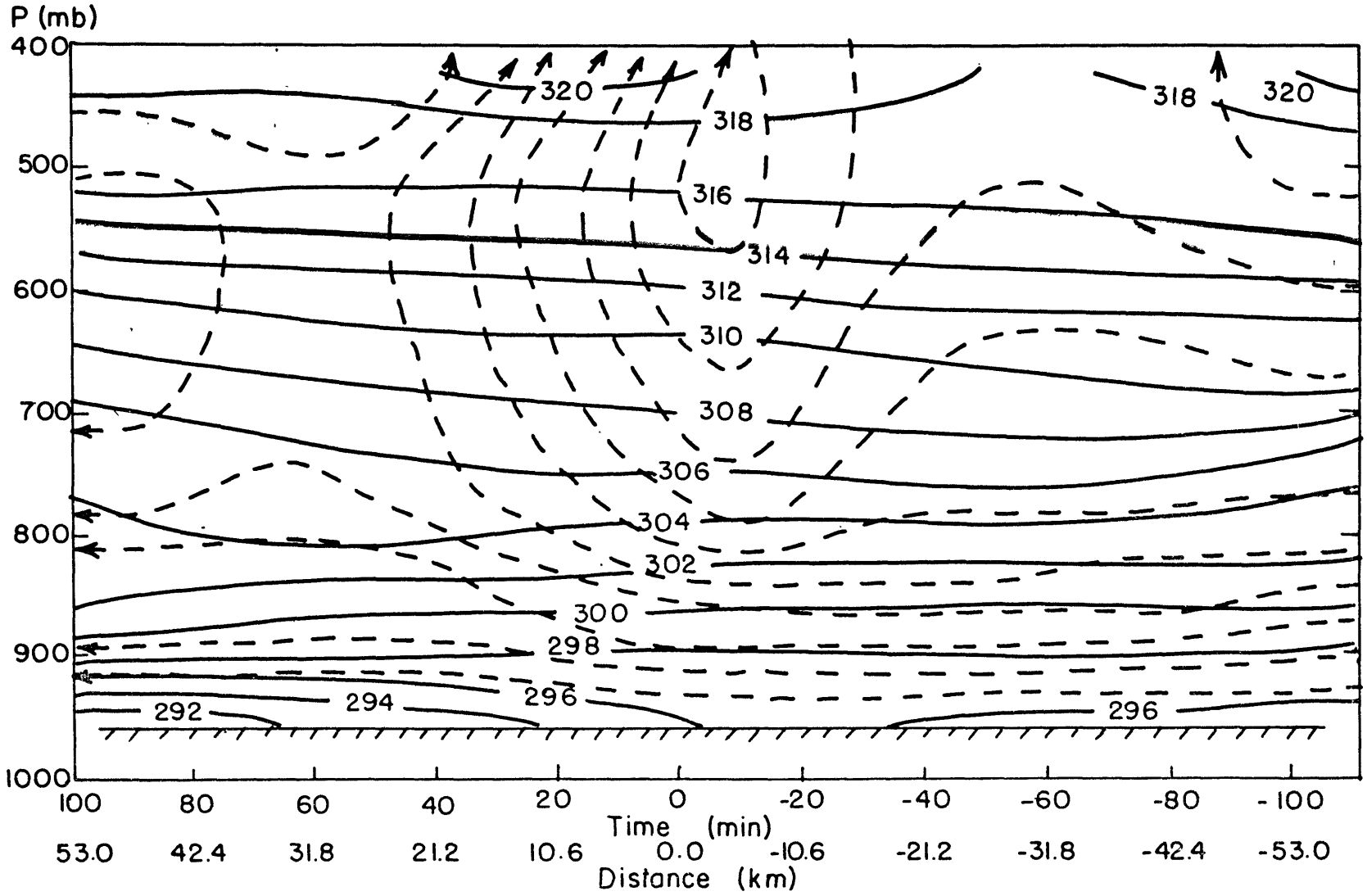
P (mb)
400
500
600
700
800
900
1000
320
318
316
314
312
310
308
306
304
302
300
298
296
294
292
318
320
296
100
80
60
40
20
0
-20
-40
-60
-80
-100
Time (min)
53.0
42.4
31.8
21.2
10.6
0.0
-10.6
-21.2
-31.8
-42.4
-53.0
Distance (km)

Fig. 23

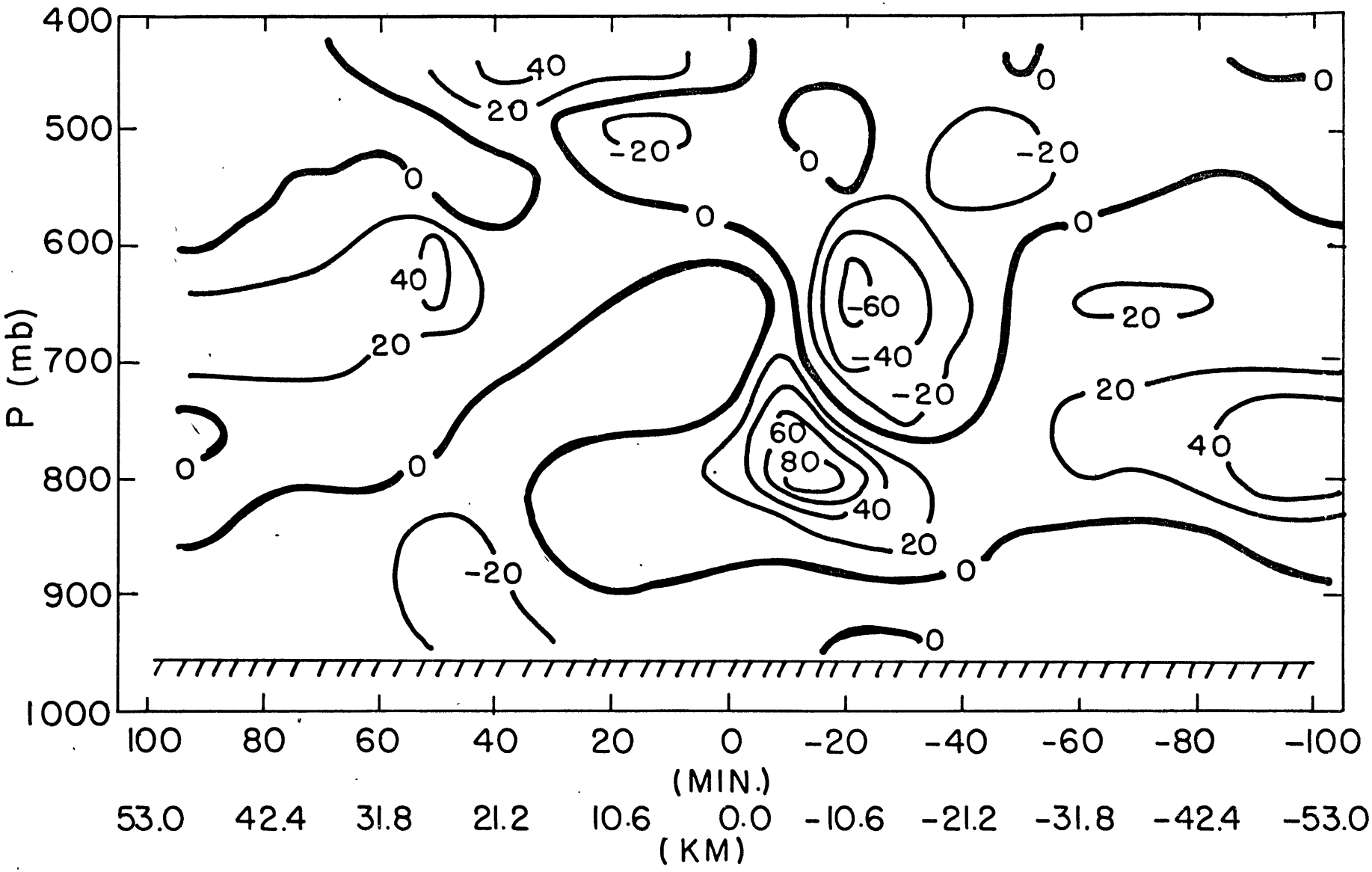
400
500
600
700
800
900
1000
P (mb)
40
20
-20
0
40
20
0
0
-20
0
0
-60
-40
-20
60
80
40
20
0
-20
0
0
-20
20
20
40
100 80 60 40 20 0 -20 -40 -60 -80 -100
(MIN.)
53.0 42.4 31.8 21.2 10.6 0.0 -10.6 -21.2 -31.8 -42.4 -53.0
(KM)

Fig. 24a

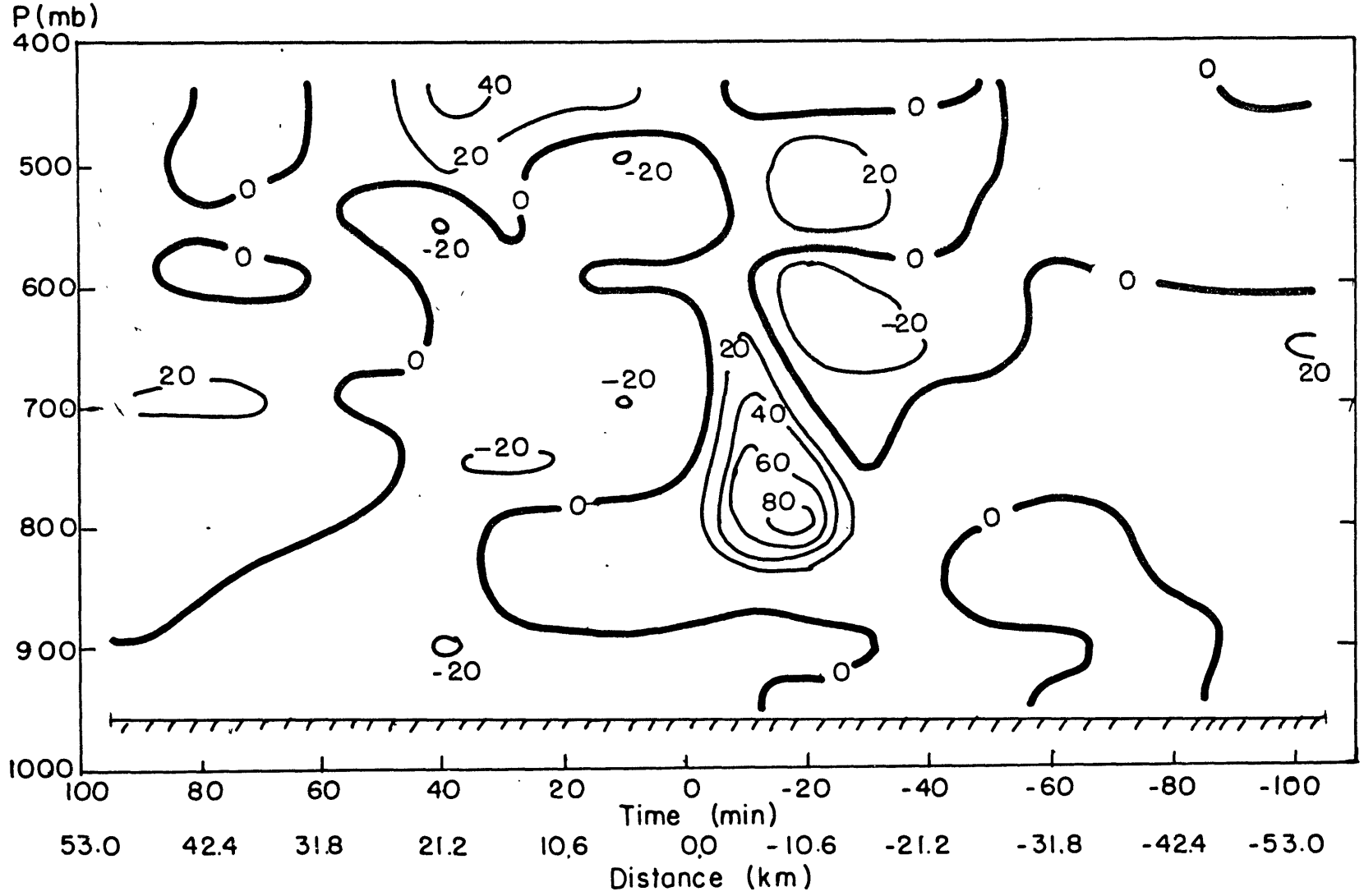
P(mb)
400
500
600
700
800
900
1000
40
20
0
-20
0
0
20
0
-20
0
0
20
0
-20
20
-20
40
60
80
0
0
0
20
-20
0
100
80
60
40
20
0
-20
-40
-60
-80
-100
Time (min)
53.0
42.4
31.8
21.2
10.6
0.0
-10.6
-21.2
-31.8
-42.4
-53.0
Distance (km)

Fig. 24b

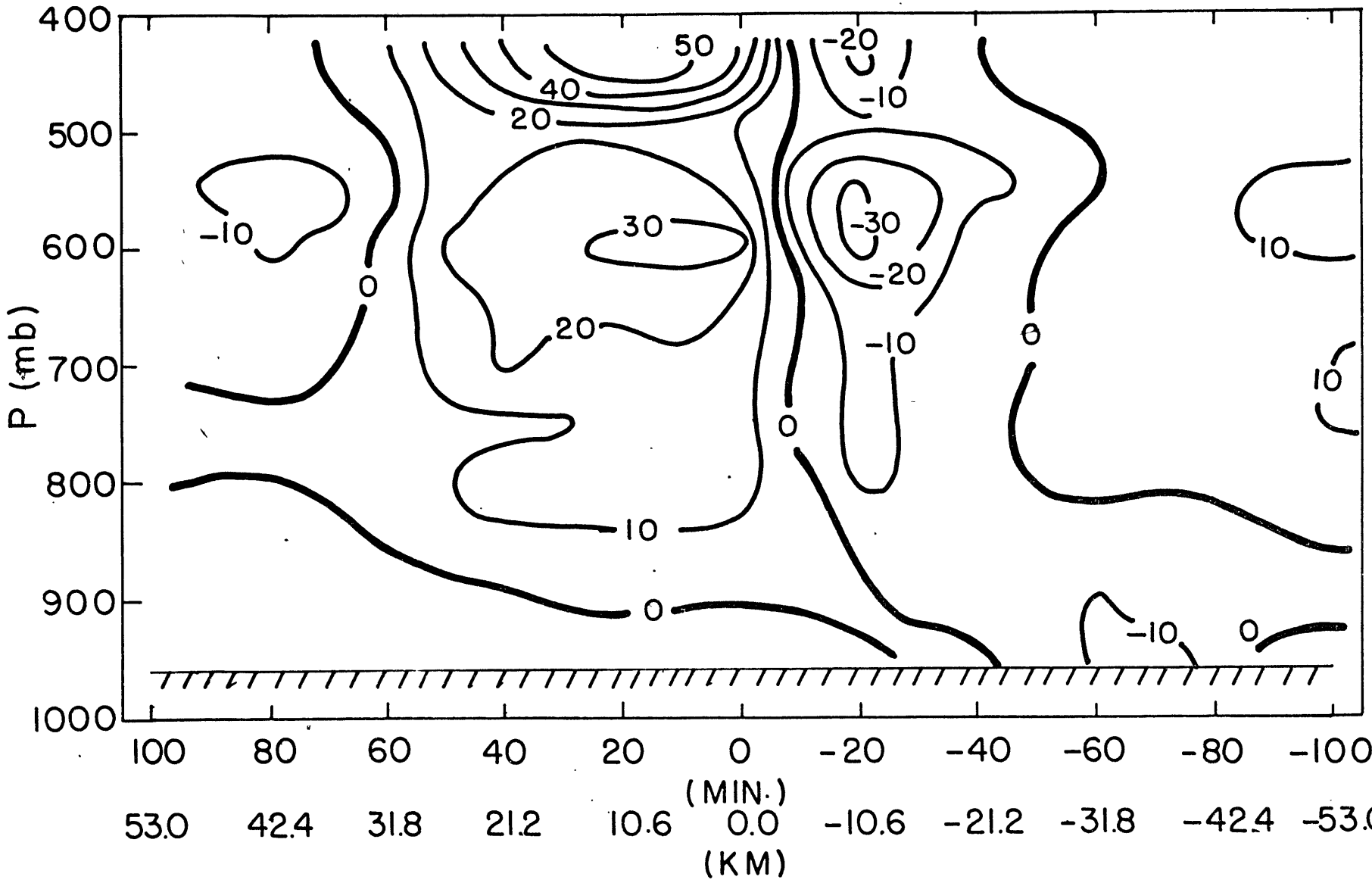
400
500
600
700
800
900
1000
P (mb)
50
40
20
-20
-10
-10
30
-30
-20
20
-10
0
0
0
10
10
10
0
-10
0
100
80
60
40
20
0
-20
-40
-60
-80
-100
(MIN.)
53.0
42.4
31.8
21.2
10.6
0.0
-10.6
-21.2
-31.8
-42.4
-53.0
(KM)

Fig. 25a

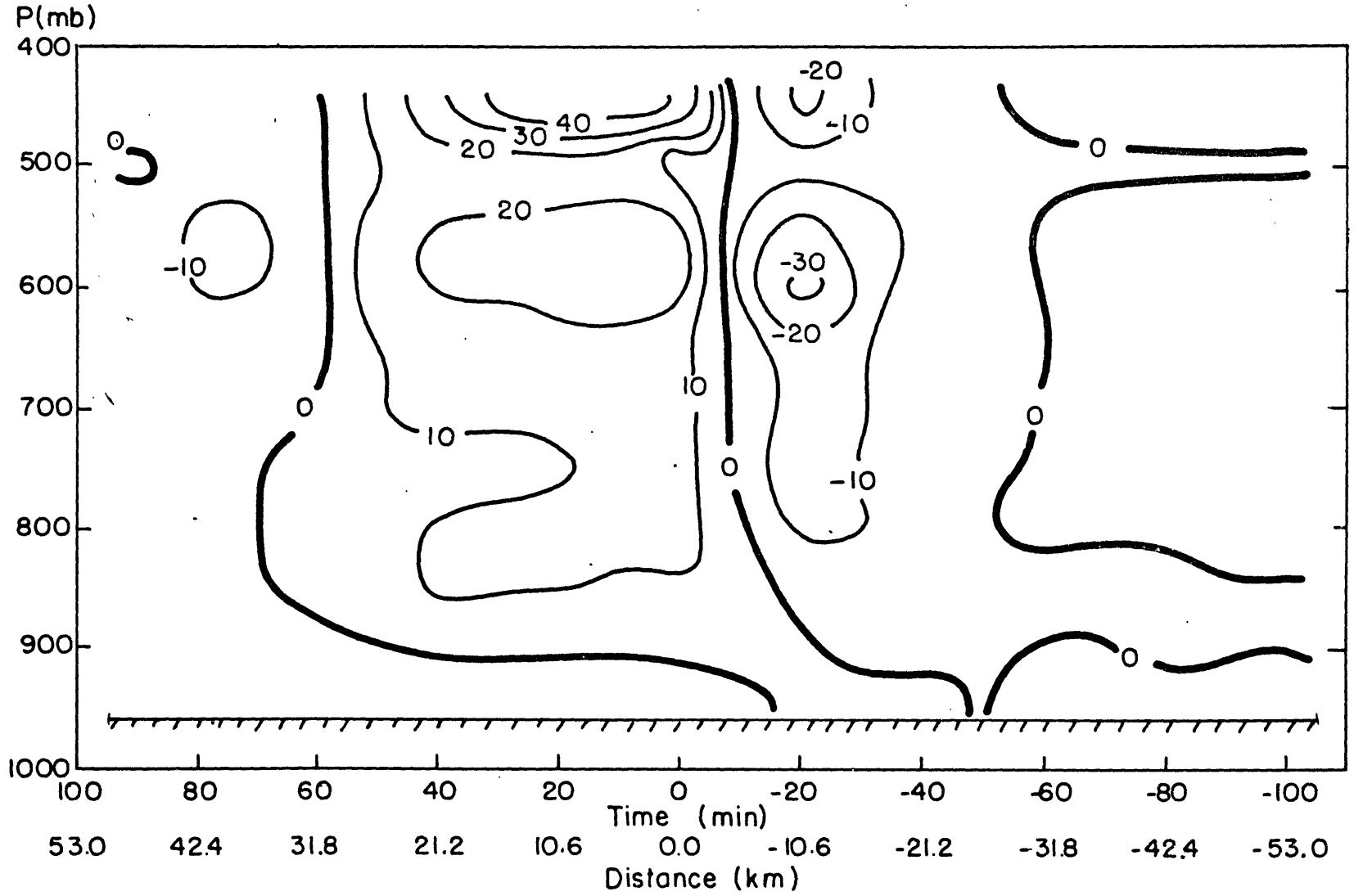
P(mb)
400
500
600
700
800
900
1000
0
-10
20
30
40
-20
-10
0
20
-30
-20
10
0
10
0
-10
0
0
100
80
60
40
20
0
-20
-40
-60
-80
-100
Time (min)
53.0
42.4
31.8
21.2
10.6
0.0
-10.6
-21.2
-31.8
-42.4
-53.0
Distance (km)

Fig. 25b

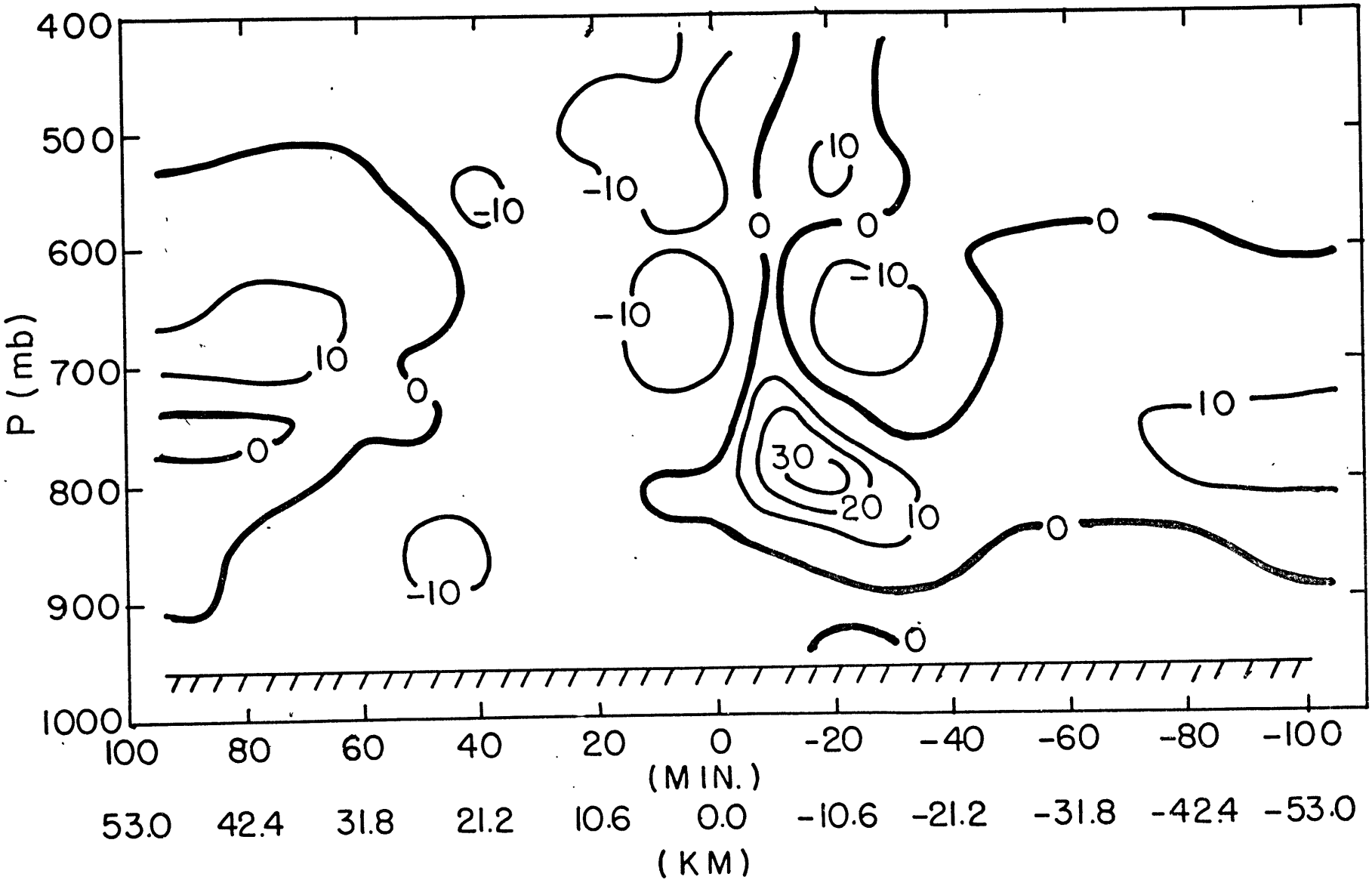
400
500
600
700
800
900
1000
P (mb)
-10
10
0
-10
-10
10
0
0
-10
0
10
30
20
10
0
-10
0
100
80
60
40
20
0
-20
-40
-60
-80
-100
(MIN.)
53.0
42.4
31.8
21.2
10.6
0.0
-10.6
-21.2
-31.8
-42.4
-53.0
(KM)

Fig. 26a

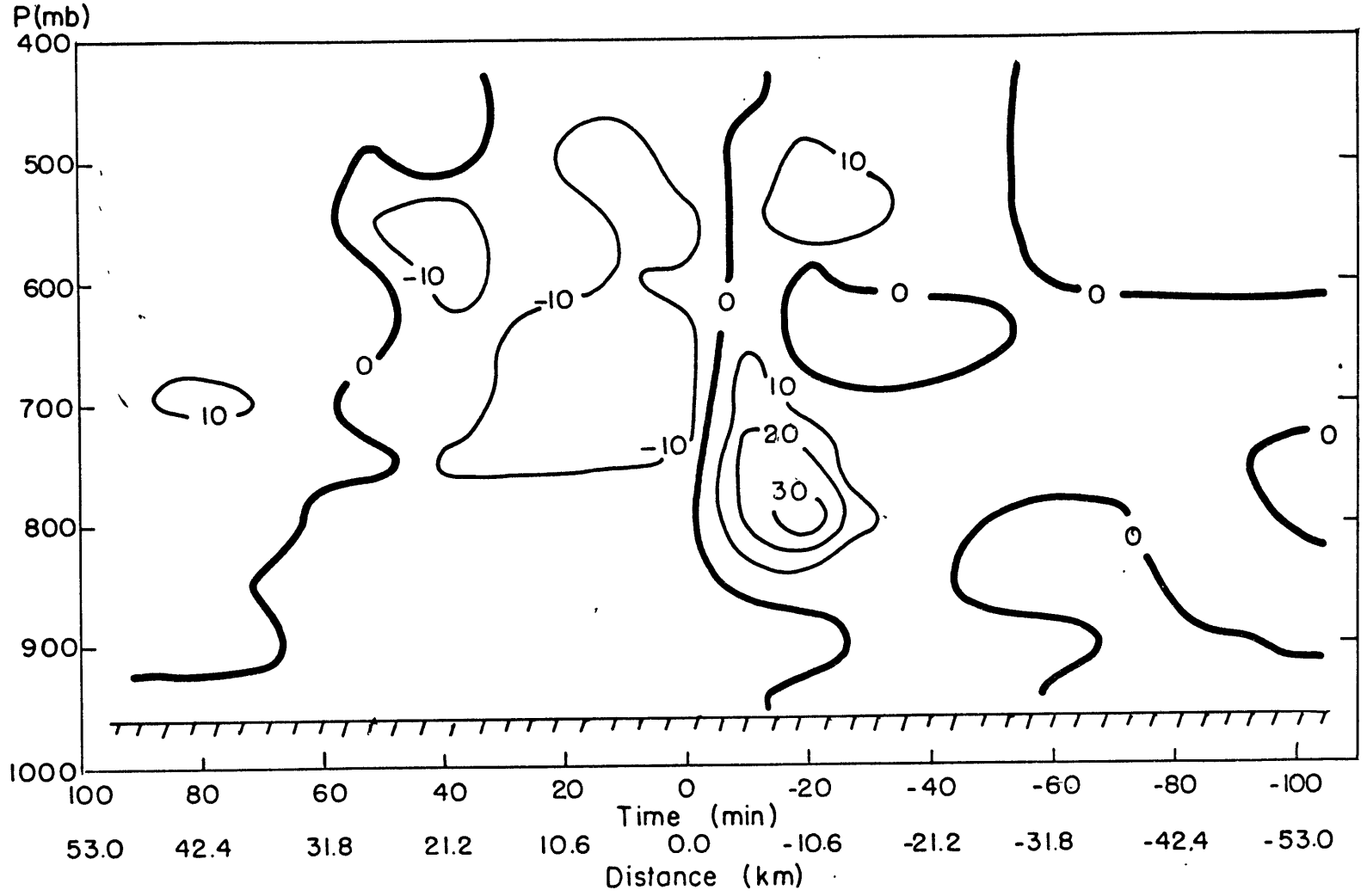
P(mb)
400
500
600
700
800
900
1000
10
-10
-10
0
10
0
0
0
10
20
30
-10
0
0
100
80
60
40
20
0
-20
-40
-60
-80
-100
Time (min)
53.0
42.4
31.8
21.2
10.6
0.0
-10.6
-21.2
-31.8
-42.4
-53.0
Distance (km)

Fig. 26b

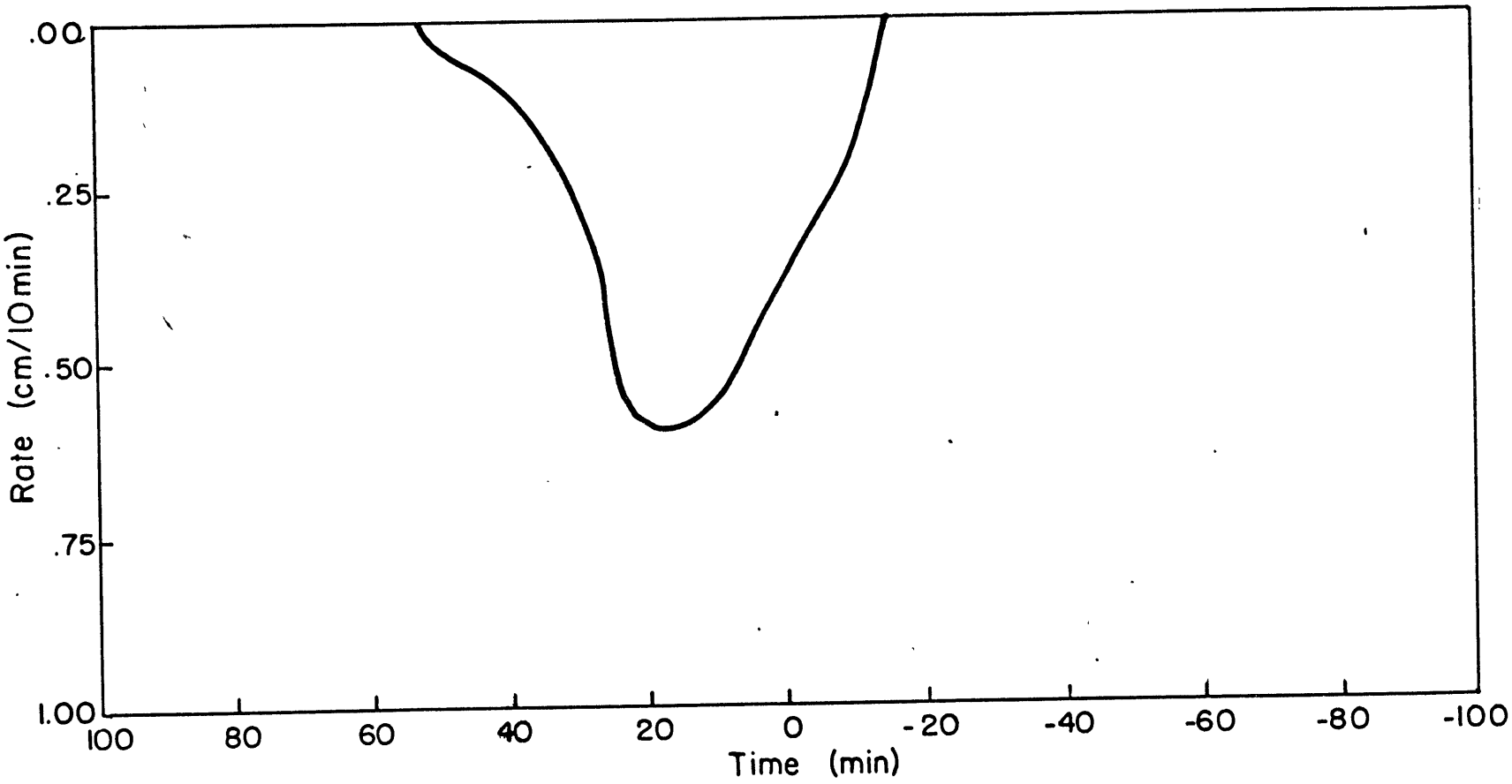
.00
.25
.50
.75
1.00
Rate (cm/10min)
100
80
60
40
20
0
-20
-40
-60
-80
-100
Time (min)

Fig. 27

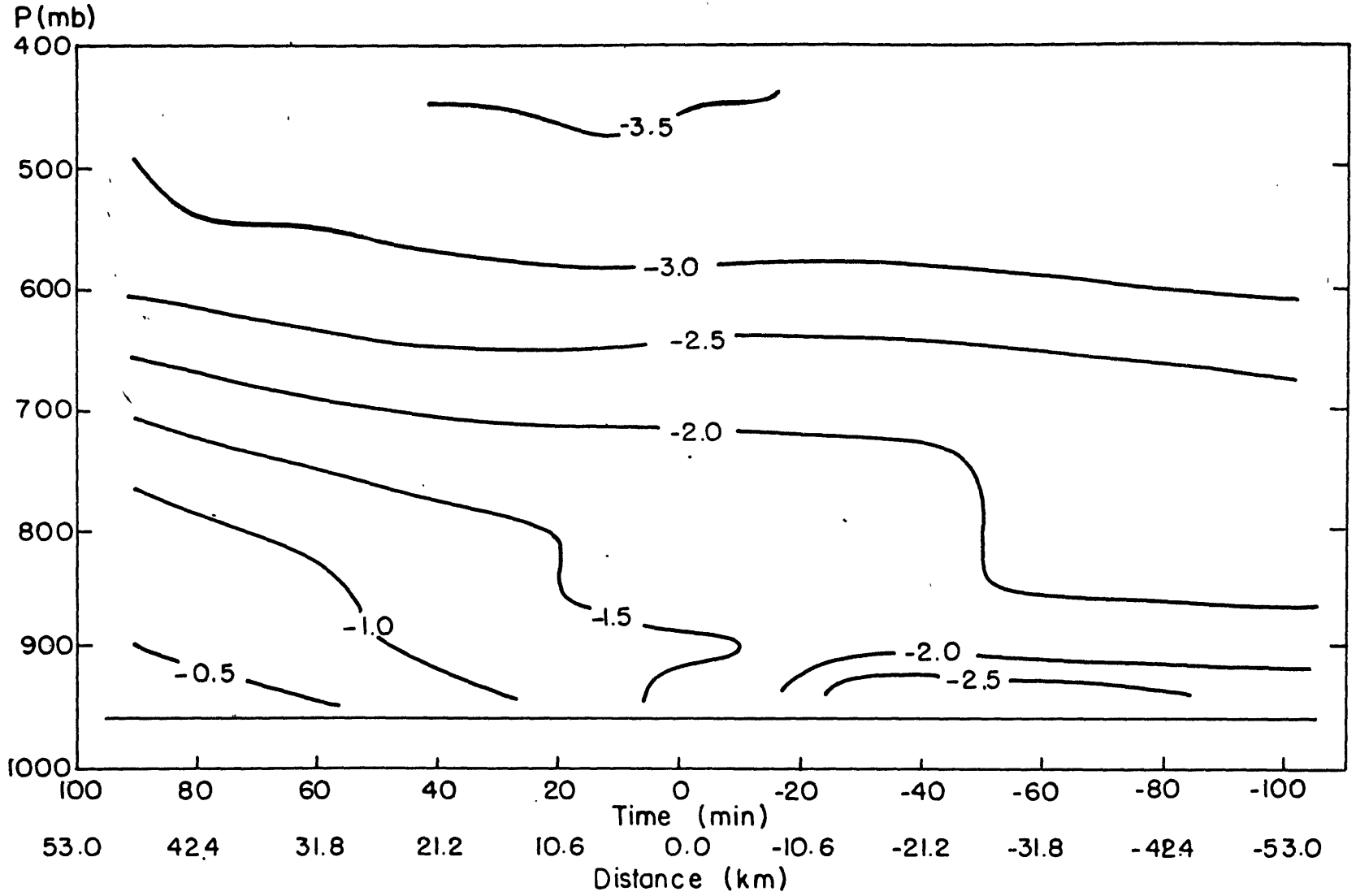
P(mb)
400
500
600
700
800
900
1000
-3.5
-3.0
-2.5
-2.0
-1.5
-1.0
-0.5
-2.0
-2.5
100
80
60
40
20
0
-20
-40
-60
-80
-100
Time (min)
53.0
42.4
31.8
21.2
10.6
0.0
-10.6
-21.2
-31.8
-42.4
-53.0
Distance (km)

Fig. 28

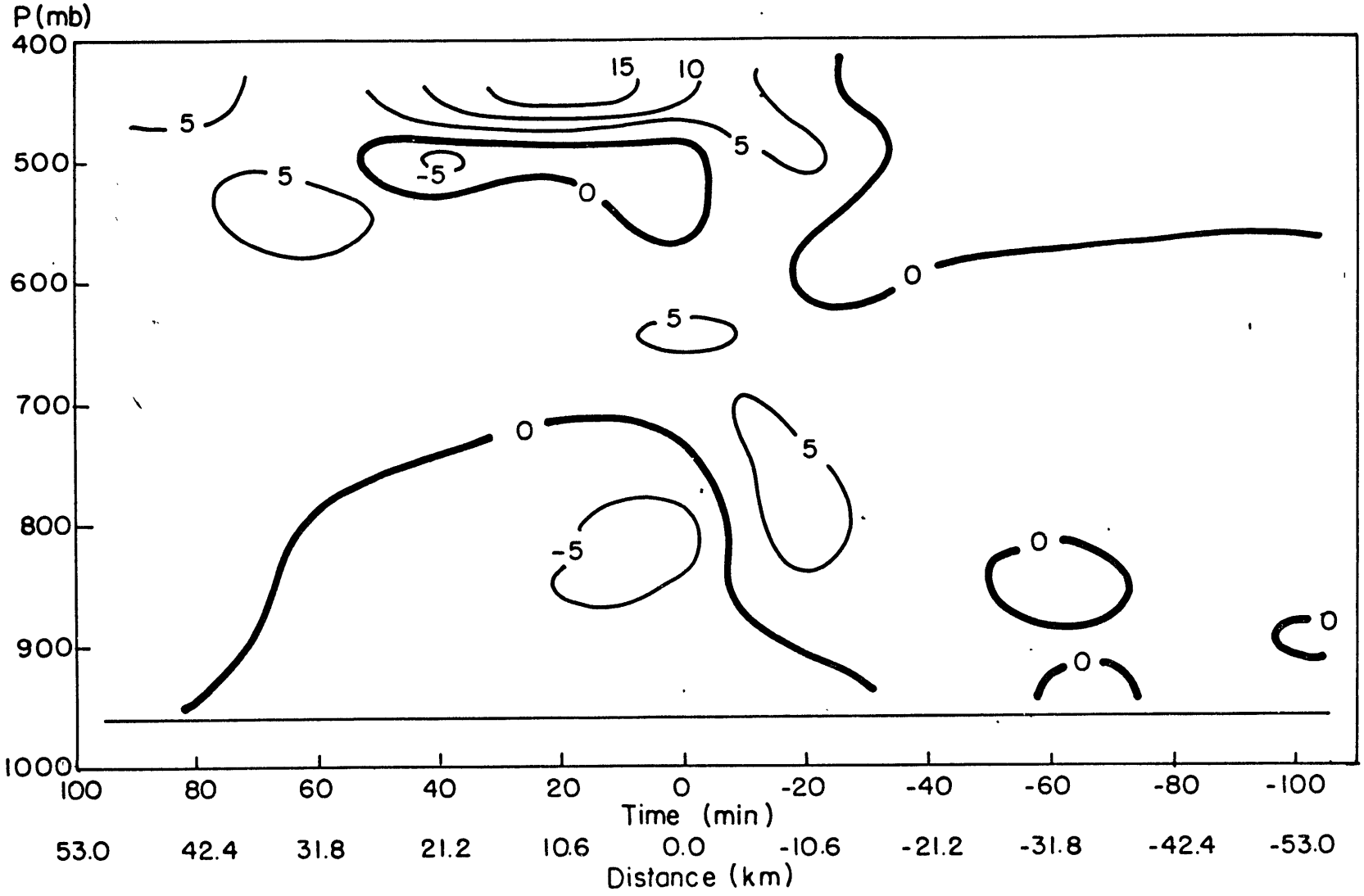
P(mb)
400
500
600
700
800
900
1000
15
10
5
5
5
-5
0
5
0
0
5
-5
0
0
0
100
80
60
40
20
0
-20
-40
-60
-80
-100
Time (min)
53.0
42.4
31.8
21.2
10.6
0.0
-10.6
-21.2
-31.8
-42.4
-53.0
Distance (km)

Fig. 29